Master's thesis

NTNU
Norwegian University of Science and Technology
Faculty of Information Technology and Electrical Engineering
Department of Electronic Systems

Erlend Kristiansen Berg

Innovative Acoustic Modules: Exploring Diffusion and Absorption for Sustainable Interior Solutions

A Study on Construction, Evaluation, and Numerical Simulation using TLM Method in Julia

Master's thesis in Electronics Systems Design and Innovation
Supervisor: Guillaume Dutilleux
Co-supervisor: Åsmund Flagstad
July 2023

NTNU
Norwegian University of Science and Technology

RAMBØLL

Erlend Kristiansen Berg

Innovative Acoustic Modules: Exploring Diffusion and Absorption for Sustainable Interior Solutions

A Study on Construction, Evaluation, and Numerical Simulation using TLM Method in Julia

Master's thesis in Electronics Systems Design and Innovation
Supervisor: Guillaume Dutilleux
Co-supervisor: Åsmund Flagstad
July 2023

Norwegian University of Science and Technology
Faculty of Information Technology and Electrical Engineering
Department of Electronic Systems

NTNU
Norwegian University of
Science and Technology

ABSTRACT

This master thesis delves into the development and evaluation of an innovative acoustical module with both diffusive and absorptive properties, intended to offer an environmentally friendly and adaptable interior solution. Combining theoretical analyses, experimental investigations, and numerical simulations using the Transmission Line Matrix (TLM) method in Julia, the thesis aims to evaluate the acoustical characteristics of the module and explore its potential applications.

The primary objectives of this research are twofold: to examine the module's acoustical properties in its two unique states (diffusive and absorptive) and to implement a TLM model within Julia to simulate the measurements performed on the physical modules. By creating a TLM model that can pre-determine the acoustical properties of the modules, the study seeks to enhance the design process and optimize the module's performance.

Through comprehensive comparisons between experimental measurements and TLM simulations, the thesis uncovers the TLM method's challenges in accurately representing certain frequencies. nevertheless, the modules demonstrate highly effective absorptive properties, with average absorption coefficient values between 100-5000 Hz surpassing 0.7. Additionally, the diffusive properties are found to be highly effective averaging diffusion coefficient values above 0.6.

Moreover, the study conducts a case study to evaluate the TLM's ability to faithfully portray acoustical behaviors within empty rooms. This case study identifies potential weaknesses and proposes methods to mitigate them, enhancing the accuracy and reliability of the TLM simulations.

This master thesis contributes valuable insights into the construction and evaluation of acoustical modules in cooperation with Ramboll corporation, utilizing advanced simulation methods and experimentation to analyze the module's performance. The findings shed light on the challenges and strengths of the TLM method and demonstrate the modules' effectiveness in both diffusion and absorption, making them promising candidates for versatile and sustainable interior design solutions. However, the implemented TLM method serve not to be a viable option for pre-determining the acoustical properties on the module and need to be further examined and developed to properly simulate the acoustical properties with high accuracy.

SAMMENDRAG

Denne masteroppgaven utforsker utviklingen og vurderingen av en innovativ akustisk modul med både diffuse og absorberende egenskaper, med sikte på å tilby en miljøvennlig og tilpasningsdyktig interiørløsning. Ved å kombinere teoretiske analyser, eksperimentelle undersøkelser og numeriske simuleringer ved hjelp av Transmission Line Matrix (TLM) -metoden i Julia, har oppgaven som mål å evaluere modulens akustiske egenskaper og utforske mulige anvendelsesområder.

De primære målene med denne forskningen er todelt: å undersøke modulens akustiske egenskaper i sine to unike tilstander (diffuse og absorberende) og å implementere en TLM-modell i Julia for å simulere målinger utført på de fysiske modulene. Ved å utvikle en TLM-modell som kan forutsi modulens akustiske egenskaper, har studien som mål å forbedre designprosessen og optimalisere ytelsen til modulen.

Gjennom grundige sammenligninger mellom eksperimentelle målinger og TLM-simuleringer, avdekker oppgaven utfordringer med å nøyaktig representere visse frekvenser ved bruk av TLM-metoden. Likevel viser modulene seg å ha svært effektive absorberende egenskaper, med gjennomsnittlige absorpsjonskoeffisienter over 0,7 i frekvensområdet 100-5000 Hz. Videre er de diffuse egenskapene også svært effektive, med gjennomsnittlige verdier over 0,6.

I tillegg gjennomfører studien en rekke tester for å vurdere TLMs evne til å gjenskape akustiske egenskaper i tomme rom. Testene identifiserer mulige svakheter og foreslår metoder for å forbedre nøyaktigheten og påliteligheten til TLM-simuleringer.

Denne masteroppgaven gir verdifulle innsikter i konstruksjon og vurdering av akustiske moduler, ved å kombinere avanserte simuleringsmetoder og eksperimenter. Resultatene belyser TLM-metodens utfordringer og styrker, og viser modulenes potensiale som allsidige og bærekraftige løsninger for interiørdesign med akustiske funksjoner. Imidlertid krever TLM-metoden videre undersøkelser og utvikling for å nøyaktig simulere akustiske egenskaper til et test objekt med høy presisjon.

PREFACE

I would like to thank my supervisors Guillaume Duttileux and Aasmund Flaggstad for irreplacable guidance and support both before, and throughout this thesis work. I will also thank Tim Cato Netland, senior engineer, for all the help and guidance given during the experimental proceedings of this thesis. Also, a huge thanks to Jarl Honningsvåg Erlien for his extensive expertise of woodworking when constructing the modules together with me an Aasmund.

I would also like to thank my family, for supporting me throughout the entirety of the time working on this thesis, as well as Patrik H. and Silje U. for several good discussions regarding the work done in this thesis. Also, my time working on this thesis was made infinitely better by Veronika.

Lastly, I would like to thank myself for doing all the work.

Si initio non successeris, ede aliquantum tortae

CONTENTS

LIST OF FIGURES

LIST OF TABLES

LIST OF LISTINGS

ABBREVIATIONS

List of all abbreviations in alphabetic order:

- **ADC** Analog to Digital Converter
- **BEM** Boundary Element Method
- **DAC** Digital to Analog Converter
- **DFT** Discrete Fourier Transform
- **EASERA** Electronic and Acoustical System Evaluation and Response Analysis
- **FD** Finite Difference
- **FEM** Finite Element Method
- **FFT** Fast Fourier Transform
- **ISO** International Organisation of Standards
- **JIT** Just-In-Time
- **LLVM** Low-Level Virtual Machine
- **NRC** Noise Reduction Coefficient
- **NTNU** Norwegian University of Science and Technology
- **QRD** Quadratic Residual Diffusor
- **STD** Standard Deviation
- **TLM** Transmission Line Matrix

TERMS AND DEFINITIONS

Sound Pressure (p)
Difference between an instantaneous total pressure and the corresponding static pressure
Note 1 to entry: Sound pressure is expressed in pascals (Pa).

Sound Pressure Level (L_p)
Ten times the logarithm to the base 10 of the ratio of the time-mean-square of a sound pressure signal to the square of the reference value. Expressed in dB.

Time-weighted Sound Pressure Level (L_{AF})
The time-weighted sound level is ten times the logarithm to the base 10 of the ratio of the running time average of the time-weighted square of a frequency-weighted sound-pressure signal to the square of the reference value [1].

Note 1 to entry: Time-weighted sound level is expressed in decibels (dB).

Note 2 to entry: For time-weighted sound level, example letter symbols are LAF, LAS, LCF, and LCS for frequency weightings A and C and time weightings F and S.

Note 3 to entry: In symbols and as an example, A-weighted and F-time-weighted sound level $LAF(t)$ at observation time t can be represented by

$$L_{AF}(t) = 10\log_{10}\left[\frac{(1(\tau_F)\int_{-\infty}^{t} p_A^2(\xi)e^{-(t-\xi)/\tau_F}d\xi}{p_0^2}\right] \qquad \text{dB}$$

where

- τ_F is the exponential time constant in seconds for the F time weighting;
- ξ is a dummy variable of time integration from some time in the past, as indicated by $-\infty$ for the lower limit of the integral, to the time of observation t;
- $p_A(\xi)$ is the A-weighted instantaneous sound-pressure signal; and
- p_0 is the reference value of 20 µPa.

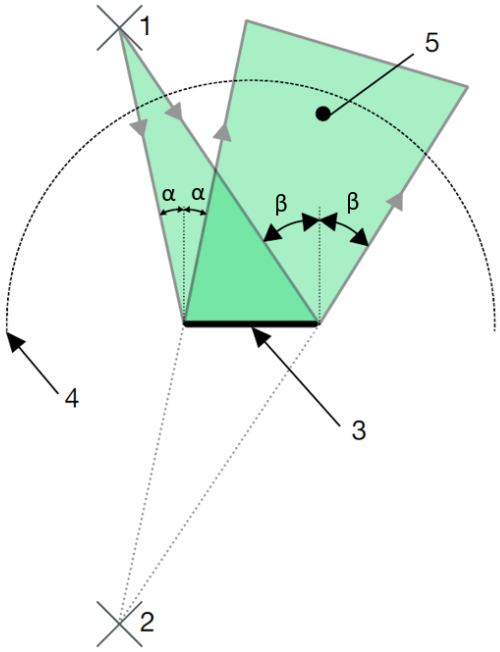

Figure 0.0.1: Specular zone representation from ISO 17497-2:2012 standard [2]. The figure illustrates the following elements: (1) source, (2) image source, (3) diffuser, (4) receiver arc, and (5) specular zone. Adapted with permission from ISO 17497-2:2012 standard [2].

Specular Zone
Area contained by imaginary lines that are constructed from the image source, which is created about the plane of a specified reference flat surface via the edges of that surface to the receiver arc or hemisphere [2].

Note 1 to entry: The reference flat surface is a plane and rigid surface, with the same projected shape or footprints as the test surface Note 2 to entry: The position at which an imaginary line from the image source to a receiver crosses the diffuser is the specular reflection point (see Figure 0.0.1).

Far Field
Region in which the reflected sound pressure level from the test surface decays by 6 dB per doubling of distance.

Note 1 to entry: In the near field, the shape of the angular field distribution is dependent on the distance from the diffuser.

Octave Bands
Octave bands are frequency bands with center frequencies that are logarithmically spaced. Each band's upper frequency is twice the lower frequency, resulting in a doubling of frequency for each octave. The center frequency of the n-th octave band is given below.
Note 1 to entry: f_0 represents the lowest center frequency of the bands.

$$f_n = 2^n \cdot f_0 \tag{1}$$

Third-Octave Bands Third octave bands are frequency bands with center frequencies that are spaced at one-third octave intervals. Similar to octave bands, the upper frequency of each band is three times the lower frequency, creating one-third octave spacing. The center frequency of the n-th third octave band is given below.

Note 1 to entry: f_0 represents the lowest center frequency of the bands.

$$f_n = 2^{n/3} \cdot f_0 \tag{2}$$

CHAPTER

ONE

INTRODUCTION

In the pursuit of sustainable and environmentally-conscious building practices, the effective utilization of recycled materials has become a significant focus in construction engineering. The acoustic properties of buildings and their interior spaces play a vital role in ensuring comfortable and conducive environments for various activities, such as music rehearsals, meetings, and workshops. Among the key elements to achieve optimal acoustics are absorptive and diffusive materials that effectively manage sound reflections and reverberations.

This thesis studies the acoustical characterization and simulation of modular absorbers constructed from recycled materials. The primary objective is to assess the potential of these modular elements in enhancing the acoustic quality of interior spaces, specifically focusing on music rehearsal rooms. The investigation involves both experimental measurements and numerical simulations, leveraging the Transmission Line Matrix (TLM) method to analyze the acoustical behavior of the modules.

1.1 Motivation

The demand for sustainable building practices has intensified the search for innovative solutions to enhance the acoustical properties of interior spaces. In response to this growing interest, the acoustic group at Ramboll Corporation has previously developed a modular interior piece, demonstrating both diffusive and absorptive properties. This rectangular box, affixed to a sliding mechanism at the top, allows for easy switching between diffusive and absorptive modes by rotating it 180°. The potential applications of such versatile modules in music rehearsal rooms, school buildings, meeting rooms, home studios, and more have sparked significant interest, prompting the need for a refined and high-performance version of these modules.

The primary objective of this thesis is to create an advanced version of the modular system with an enhanced ease-of-use factor, capable of seamlessly switching between diffusive and absorptive states. To achieve this, a thorough investigation into the acoustical properties of the modules will be conducted. The use of Transmission Line Matrix (TLM) method, implemented in the programming language Julia, will facilitate the simulation of these acoustical properties. By simulating

the modules' behavior prior to their construction and validating the simulation results against actual measurements, the reliability and accuracy of the TLM as a simulation tool will be assessed.

Through a comprehensive analysis of the TLM simulations and experimental measurements, this study aims to offer valuable insights for optimizing the design and functionality of the modules for acoustic engineering applications, as well as contribute to sustainable building practices.

1.2 Outline of the Thesis

This thesis is written for Ramboll corporation, aimed at creating a versatile product for future building projects. It is important to note that this thesis does not contain any sections that disclose sensitive information related to Ramboll. Instead, the focus is primarily on exploring relevant theoretical aspects of the simulation tool, acoustical measurement techniques, and the construction of the modular module. The goal is to develop a comprehensive understanding of the subject matter and propose innovative solutions without compromising any proprietary information.

First, the thesis will introduce the required theory for discussing the methods and results. The Theory chapter contains fundamental information regarding acoustical parameters, post-processing tools, diffusors and theory on the simulation method. The last subsection is intended to provide the reader with information regarding uncertainty factors related to measurements and the results gathered.

The object of the Methodology chapter is to provide the reader with the information necessary to recreate the results of this thesis. It outlines the procedures employed to create the modules using recycled materials and the measurement techniques used to assess their acoustical properties. Additionally, it details the implementation of the TLM as a simulation tool to predict the absorbers' performance.

The purpose of the Results and Discussion chapter is to describe and present the findings of the simulations described in the Methodology chapter. The results obtained from both the experimental measurements and the numerical simulations are presented and thoroughly analyzed. A comprehensive comparison between the measured and simulated results is made to assess the accuracy and reliability of the TLM method for this specific application. A deeper look into the TLM method and its weaknesses is also discussed, resulting in the findings of valuable information regarding selection of parameter values for research at a given frequency range.

Drawing from the findings in the Results and Discussion chapter, the Conclusion chapter highlights the main outcomes of the study and their implications. The effectiveness of the modules in managing sound absorption and diffusion is evaluated, along with the limitations of the TLM method as a simulation tool for predicting acoustical properties.

Lastly, building upon the current investigation, the Future Work chapter identifies potential areas for further research and improvements. The integration of advanced data processing techniques and software compatibility, such as CAD software and the Julia package GMSH, are proposed to enhance the accuracy and

efficiency of the TLM simulations. Additionally, future studies may focus on optimizing the design of the modules to reduce weight while preserving their acoustical effectiveness.

CHAPTER

TWO

THEORY

This chapter provides the necessary theoretical foundation for understanding the research presented in this thesis. It includes an overview of the basic principles of acoustics, the relevant theory behind the programming language used for simulating the modules, and the post-processing methods applied to the collected measurement data, which ultimately affect the level of uncertainty in the measurement results.

The propagation of acoustic waves has been thoroughly studied in the literature, and the fundamentals will not be discussed here. For an introduction, interested readers, as well as readers with no expertise in acoustics, might consult Kinsler et al. [3] or Beranek and Mellow [4]. There exist however a few acoustical properties that will be touched upon.

2.1 Scattering

Acoustic scattering, a central aspect in acoustics, involves the interaction of sound waves with objects in their path, causing changes in direction and propagation. The phenomenon is akin to the scattering of light waves by particles or surfaces [5]. When acoustic waves encounter obstacles, scattering can manifest in various forms depending on the object's size, shape, composition, and the sound wave's frequency and angle of incidence.

Scattering leads to the random redirection of sound waves, causing energy to spread in different directions upon encountering irregularities or small objects. This phenomenon plays a crucial role in acoustics and finds comprehensive explanations in well-regarded acoustics references, such as Pierce's "Acoustics: An Introduction to its Physical Principles and Applications" [6], Kuttruff's "Acoustics: An Introduction" [7], Morse and Ingard's "Theoretical Acoustics" [8], and Beranek's "Acoustics" [9]. These references offer valuable insights into various scattering phenomena, encompassing reflection, diffraction, scattering, and absorption.

2.1.1 Directivity

In practical measurements, understanding how sound is scattered by an object becomes crucial. The sound pressure level variation around the object in different

directions is of interest. This is analogous to the concept of directivity, where the sound pressure level is not equal in all directions at a certain distance away from the scattering object [10].

For objects with variations in the medium in only one direction, such as one-dimensional diffusors, the directivity is typically considered in the profile plane for the diffusor.

To describe directivity, the directivity factor is often used. It represents the ratio between the intensity at a given distance on a chosen reference axis and the averaged intensity emitted by the same loudspeaker in all directions [11]. The directivity factor, denoted as Q, can be calculated using the following equation [12]:

$$Q = \frac{|D|^2_{ref}}{\left\langle |D|^2 \right\rangle} \tag{2.1}$$

Here, D^2_{ref} represents the sound pressure response caused by sound coming from the reference direction. In acoustics, the reference direction is the predefined direction with respect to which we measure and evaluate the sound radiation pattern. Typically, the reference direction is chosen as the direction of normal incidence, which means the sound waves are incident perpendicular to the measurement point's surface.

To calculate the directivity factor, the squared sound pressure response at the reference direction with the average squared sound pressure response obtained from all possible angles of incidence ($\left\langle |D|^2 \right\rangle$). The intensity of sound is proportional to the square of the sound pressure, which is why the quantities are squared [13]. The measured sound pressure, represented by D, is used to analyze the directivity pattern, to assess how much sound energy is directed in the reference direction compared to the overall sound radiation.

2.1.2 Directional Diffusion Coefficient

The directivity index is a parameter used to quantify the directional characteristics of a sound source, providing insight into how the sound energy radiated by the source is distributed in space. A higher directivity index indicates a more focused and directional source, while a lower value suggests a more omni-directional sound field. Expressed in decibels (dB), the directivity index is calculated as the difference between the sound pressure level at the reference angle and the average sound pressure level over a specified angular range, as shown in Equation (2.2)). It offers a concise representation of the spatial characteristics of a sound source and is directly related to the directivity factor. The directivity index is frequency-dependent [12], where f denotes the third-octave bands.

$$DI(f) = 10 \cdot \log_{10}\left(Q(f)\right) \tag{2.2}$$

The directional diffusion coefficient (d_θ), defined in ISO 17497:2012 [2], describes the directionality of a scattering surface. For a fixed source position and in each one-third-octave band, the directional diffusion coefficient can be calculated from the set of third-octave sound pressure levels (L_i) measured at n receivers using Equation (2.3). This equation evaluates the difference between the sum of

the squared sound pressure levels and the squared sum of each sound pressure level, divided by the product of the number of receivers minus one and the sum of the squared sound pressure levels.

$$d_\theta = \frac{\left(\sum_{i=1}^{n} 10^{L_i/10}\right)^2 - \sum_{i=1}^{n} \left(10^{L_i/10}\right)^2}{(n-1)\sum_{i=1}^{n} \left(10^{L_i/10}\right)^2} \tag{2.3}$$

2.2 Reflection

Reflection is a fundamental phenomenon in acoustics that occurs when sound waves encounter rigid surfaces or boundaries between different media. The law of reflection, as described in standard acoustics textbooks [6, 7], states that the angle of incidence is equal to the angle of reflection. This process shares similarities with the reflection of light waves when encountering rigid surfaces or media boundaries, where incident waves undergo the reflection of energy [5]. The law of reflection governs this process, stating that the angle of incidence is equal to the angle of reflection [6, 7], which is illustrated in Figure 2.2.1 along with examples of absorption and diffraction.

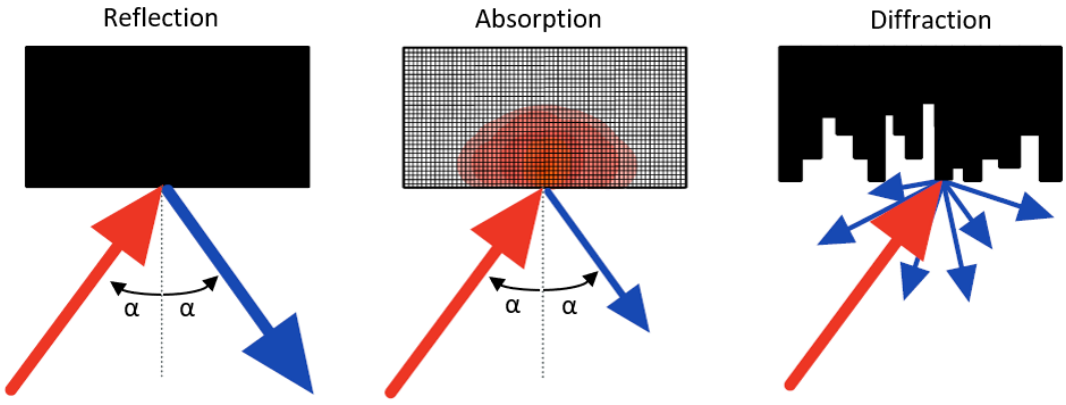

Figure 2.2.1: Reflection, absorption and diffraction illustrated from left to right. The red arrows indicate the incident pulses while the blue indicate the reflected pulses. The red color inside the boundary in the absorption example indicate heat as a result of absorption. α indicate the incident and reflected angle given by the law of reflection.

2.2.1 The Law of Reflection

The law of reflection states that the angle of incidence is equal to the angle of reflection. This law arises from the conservation of energy and momentum during the reflection process. According to the law of reflection, the incident wave and the reflected wave are symmetrical with respect to the normal line drawn at the point of incidence [5, 6]. The angles of incidence and reflection are measured relative to this normal line.

2.2.2 Reflection Coefficient

The reflection coefficient in acoustics quantifies the amount of energy reflected by a surface or interface, defined as the ratio of reflected wave amplitude to incident wave amplitude [14]. This coefficient depends on factors such as the properties of the reflecting surface, angle of incidence, and acoustic impedance mismatch between the media.

Surface roughness significantly influences acoustic wave reflection, scattering incident waves in multiple directions, resulting in diffuse reflection [14]. The degree of surface roughness affects the scattering pattern and distribution of reflected energy.

Reflection characteristics are also impacted by the angle of incidence. At normal incidence, the reflection coefficient primarily depends on the acoustic impedance mismatch between the media. However, at oblique angles, additional factors like polarization effects and phase changes come into play, necessitating the use of vector calculus and complex mathematical formulations for analysis [14].

Acoustic impedance, representing sound wave transmission resistance, influences the magnitude of reflection at interfaces with different acoustic impedances [14, 15]. The calculation of reflection coefficients involves employing Fresnel equations that incorporate the acoustic impedance values of the media.

2.3 Diffraction

When a sound wave encounters an edge or an object, the point of the edge or an object act as a new point source spreading sound energy in all directions, and this phenomenon is called diffraction. As the sound wave interact with the edges or corners of these objects or openings, they diffract, changing direction and spreading into the region behind the obstacle. The extent of diffraction depends on various factors, including the wavelength of the sound, the size and shape of the obstacle or opening, and the characteristics of the surrounding medium. When the wavelength is significantly larger than the size of the object or opening, the diffraction effects are minimal. However, when the wavelength and the size of the obstacle or opening are comparable, diffraction becomes more pronounced. The principle of diffraction are explained in detail in references such as Kuttruff's "Acoustics: An Introduction" [7] and Rossing and Fletcher's "Principles of Vibration and Sound" [9].

2.4 Absorption

Absorption is a significant phenomenon in acoustics, occurring when sound waves interact with materials or objects, leading to the conversion of sound energy into other forms, such as heat. The level of absorption is influenced by the material properties and the frequency of the sound wave. A comprehensive exploration of this subject is available in Pierce's "Acoustics: An Introduction to its Physical Principles and Applications" [6].

When sound waves encounter a material or surface capable of dissipating sound energy, absorption takes place. This dissipation occurs through various mech-

anisms, including air friction, molecular interactions, and material resonances. Upon striking an absorptive surface, a portion of the sound energy is absorbed, leading to reduced sound reflection and transmission. The absorption properties of materials are quantified using coefficients, such as the Sound Absorption Coefficient (α) or the Noise Reduction Coefficient (NRC). α measures the fraction of incident sound energy absorbed by a material at a particular frequency, while NRC provides an average absorption value across a range of frequencies.

2.5 Reverberation Time and Sabine-Eyrings Equation

Reverberation time is a fundamental parameter in room acoustics that quantifies the decay of sound in a space after the source has ceased. It plays a crucial role in determining the subjective perception of sound quality, speech intelligibility and the overall acoustic characteristics of a room. Sabine-Eyrings equation, derived by Wallace Clement Sabine and Carl Eyring, provides a theoretical framework for calculating reverberation time based on the physical properties of the room and its contents [16]. Sabine-Eyrings equation relates the reverberation time, D_R, to the volume, V, and the total absorption, A, within a room as shown in Equation (2.4).

$$D_R = \frac{0.16 \cdot V}{S\,(1 - R^2)} \tag{2.4}$$

The equation assumes a diffuse sound field in the room with uniform distribution of absorption. Total absorption includes coefficients of all surfaces, such as walls, ceiling, floor, and objects. Reverberation time is measured in seconds (s) using methods like EDT, $T10$, $T20$, and $T30$ [15]. $T10$ represents the reverberation time based on a 10-decibel decay, $T20$ for a 20-decibel decay, and $T30$ for a 30-decibel decay. EDT reflects the reverberation time based on a 10-decibel decay from the initial level.

For $T10$, $T20$, and $T30$, the sound pressure level drops 5 dB before extrapolating the linear decay time from their respective ranges. For instance, $T20$ measures the time it takes for the sound pressure level to drop from 5 dB to 25 dB, and then extrapolates to the time it takes to drop 60 dB.

To accurately calculate the reverberation time using Sabine-Eyrings equation, knowledge of the absorption coefficients of the materials and surfaces in the room is essential. The equation can also be used to find the absorption coefficient by measuring the reverberation times. Standardized methods such as the reverberation chamber method [1] or the impedance tube method [17] can be used. It is important to note that Sabine-Eyring's equation assumes certain simplifications and idealizations, such as a diffuse sound field and uniform absorption distribution. In reality, rooms often have a non-uniform absorption characteristics due to the presence of furniture, people and other objects. Therefore, the calculated reverberation time may deviate from the actual observed values in practice.

2.6 Acoustical Signal Processing

This chapter investigates the theoretical aspects of data processing techniques used on measurements obtained from the reverberation and anechoic chambers. The aim is to determine the directional diffusion coefficient and absorption coefficient. Within these chambers, sound waves are converted into electrical signals through microphones [18]. These signals are subsequently sampled and digitized by an analog-to-digital converter (ADC). Measurement software then interprets the digital signals to generate the impulse response, which can be further analyzed [19].

2.6.1 System Behaviour and Analysis in the Time- and Frequency Domain

In the field of acoustics, understanding the behavior of a linear and time-invariant (LTI) system is vital to establish the relationship between input and output signals [20]. When measuring sound waves that are reflected from objects, the measurement system functions as an LTI system. The input of this system corresponds to the actual sound waves resulting from the object's scattering, while the output represents the discretized measurement obtained through the measurement software.

Linearity characterizes a system's behavior by its consistent response, irrespective of changes in input power [21]. This property can also be understood in terms of obeying the principles of superposition [22]. Time-invariance, on the other hand, implies that the system's characteristics remain constant over time [22].

The relationship between the input and output of a system is typically represented by either the impulse response or the transfer function, depending on whether it is expressed in the time domain or frequency domain. This relationship can be mathematically described through convolution [23] in the time domain or multiplication in the frequency domain, as depicted in Equation (2.5).

$$\begin{aligned} g(t) &= s(t) * h(t) \\ G(f) &= S(f) \bullet H(f) \end{aligned} \tag{2.5}$$

In the above equations, the variable t represents the time parameter in the time domain, while f denotes the frequency parameter in the frequency domain. The lowercase variables $s(t)$ and $g(t)$ represents, respectively, the input- and output signals in the time domain, while the uppercase equivalent $S(f)$ and $G(f)$ is the same parameters in the frequency domain. $h(t)$ represents the impulse response, and $H(f)$ represents the transfer function. The capitalized variables indicate the equivalent system parameters to their lowercase counterparts in the time domain.

2.6.2 Fourier Transform and Fast Fourier Transform

The Fourier Transform is a mathematical tool widely used in signal processing and spectrum analysis to analyze the frequency content of a time-domain signal. It allows us to decompose a signal into its constituent frequencies and obtain a

representation in the frequency domain. The Fast Fourier Transform (FFT) is an efficient algorithm used to compute the Fourier Transform of a discrete signal. The Fourier Transform of a continuous-time signal $x(t)$ and the Discrete Fourier Transform of a discrete-time signal $x[n]$ is defined as follows.

Continuous Fourier Transform:

$$X(f) = \int_{-\infty}^{\infty} x(t) \cdot e^{-j2\pi ft} dt \tag{2.6}$$

Discrete Fourier Transform:

$$X[k] = \sum_{n=0}^{N-1} x[n] \cdot e^{-j2\pi kn/N} \tag{2.7}$$

In these equations, $X(f)$ represents the complex spectrum of the signal, where f denotes the frequency. $X[k]$ represents the complex frequency spectrum at the discrete frequency k, while $x[n]$ denotes the complex-valued input sequence at time index n for the discrete-time signal. The parameter N represents the number of samples in the input sequence.

For discrete signals, the Fourier Transform is computed using the Discrete Fourier Transform (DFT), which can be efficiently implemented using the FFT algorithm. The FFT reduces the computational complexity of the DFT from $O(N^2)$ to $O(N\log_2 N)$, where O represents the "order of" or "big O" notation. In this context, N refers to the number of samples in the input signal and the logarithm used in the complexity analysis is the base-2 algorithm [24].

The computational complexity of the DFT as $O\left(N^2\right)$ implies that the number of mathematical operations required for computing the DFT grows quadratically with the number of samples. However, the FFT algorithm reduces this complexity to $O\left(N\log_2 N\right)$, resulting in significantly faster computation times, especially for large input sizes. This efficiency has made the FFT algorithm widely used in various applications, including real-time signal processing and spectrum analysis [25]. The resolution of frequency components obtained through an FFT is determined by the number of samples and the sampling rate of the input signal. The frequency resolution, denoted as Δf, is given by:

$$\Delta f = \frac{f_s}{N} \tag{2.8}$$

In this equation, Δf represents the minimum frequency separation that can be resolved, f_s is the sampling rate, and N is the number of samples. Increasing the number of samples, or the sampling rate, improves the frequency resolution, allowing finer distinctions between adjacent frequency components. This enhanced resolution is particularly evident in frequency responses, displayed with a logarithmic frequency axis, especially at the lower frequency range. A low frequency resolution in this region results in less detailed responses for lower frequencies [26].

2.6.3 Impulse Response Measurements

The impulse response describes the behavior of a system or a room in response to a given input, often an impulsive input such as the Dirac delta function or a sweep. The Dirac delta function, denoted as $\delta(t)$, is a mathematical construct that

represents an idealized impulse with an infinitesimally short duration and infinite amplitude. Mathematically, the impulse response $h(t)$ represents the system's output $y(t)$ resulting from the input $x(t)$ through a convolution, as shown in Equation (2.5), where * denotes the convolution operation.

The impulse response captures the system's time-domain behavior, illustrating how it responds to different frequencies and the presence of resonances or decays. It contains information about the system's amplitude, phase, and duration. Measurements of impulse responses are typically conducted using specialized equipment such as omnidirectional microphones and a starter pistol, impulse generator or a speaker with a given source signal. By recording the response of a room to the given sound source, the impulse response can be analyzed and further processed.

2.6.3.1 Logarithmic Sweep

One of the stimulus methods for the impulse response is a sweep. The system is driven by a sinusoidal signal with a frequency that is slowly increased to sweep through the frequency range of interest [27]. Sweeps exist in different designs, but the ones of interest is the logarithmic and linear. Linear sweeps increase the sinusoidal frequency linearly per time interval, which is referred to as white colourisation, meaning that all frequencies are equally represented. As a result, the energy is evenly distributed across the frequency spectrum, leading to a flat frequency response. White noise is an example of a signal with white coloration. The logarithmic sweep on the other hand doubles per time interval, which is known as a pink excitation signal. This refers to a frequency response where the power spectral density decreases by 3 dB per octave, meaning every doubling of frequency. In a logarithmic sweep, the frequency increases exponentially while the amplitude remains constant. This results in a decreasing power spectral density.

The releationship between the power spectral density and frequency in pink noise can be mathematically expressed as

$$S(f) \propto \frac{1}{f^{\alpha}} \tag{2.9}$$

Here, $S(f)$ represents the power spectral density at frequency f, and α is the scaling factor associated with the specific pink noise variant [24].

2.6.4 Tukey Window

In signal processing and spectral analysis, the Tukey window, also known as the tapered cosine window, is a widely used function for smoothing and shaping the spectrum of a signal. It is a form of a window function that modifies the Fourier Transform of a signal to reduce the adverse effects of spectral leakage and improve frequency resolution [28].

The Tukey window is characterized by a combination of the rectangular window and the cosine window, governed by a shape parameter α. When α is set to zero, the Tukey window reduces to a rectangular window, and when α is set to one, it becomes a pure cosine window resembling half a period of a cosine wave.

The mathematical expression for the Tukey window $w[n]$ of length N is given by [29]:

$$f(n) = \begin{cases} \frac{1}{2}\left[1 + \cos\left(\pi \frac{n - \frac{N-1}{2}}{\alpha\left(\frac{N-1}{2}\right)}\right)\right] & \text{for } |n - \frac{N-1}{2}| \leq \frac{\alpha(N-1)}{2} \\ 1 & \text{for } |n - \frac{N-1}{2}| > \frac{\alpha(N-1)}{2} \end{cases} \tag{2.10}$$

Here, n represents the index of the window sample, ranging from 0 to $N-1$. N denotes the window's length, and α is the shape parameter, constrained to values between 0 and 1. The parameter α governs the trade-off between resolution and side-lobe levels of the window. Smaller α results in a wider main lobe, offering improved frequency resolution but higher side-lobe levels. Conversely, larger α narrows the main lobe, providing better side-lobe suppression while potentially sacrificing frequency resolution.

The Tukey window is a versatile tool in digital signal processing applications, finding broad use in spectral analysis and various other tasks. By incorporating the Tukey window into the input signal in the TLM grid, noise presence is mitigated due to the guaranteed smooth start and end points.

2.6.5 Lowpass Filter

A lowpass filter is a fundamental concept in signal processing and acoustics. It is designed to allow low-frequency components of a signal to pass through while attenuating or removing higher-frequency components. In the context of acoustics, lowpass filters are commonly used to shape the frequency response of audio systems, speakers, and acoustic modules.

The lowpass filter is characterized by its cutoff frequency, which defines the point where the filter starts attenuating higher frequencies. Frequencies below the cut-off pass through with minimal alteration, while frequencies above the cutoff are progressively reduced. The area below the cut-off is called the passband.

Mathematically, a lowpass filter is represented by a transfer function that describes the frequency response. The simplest form of a lowpass filter is the first-order lowpass filter, also known as a "single-pole" filter. It is characterized by a -6 dB per octave roll-off, which means the signal level decreases by 6 dB for every doubling of frequency after the cutoff frequency [30].

By selectively allowing low frequencies to pass through, lowpass filters can shape the sound characteristics of a space or device, improving clarity and reducing unwanted noise. One common implementation of a lowpass filter is the Butterworth filter, which has a flat frequency response in the passband and a smooth roll-off beyond the cutoff frequency [30]. The Butterworth filter is designed to minimize distortion and phase shift in the passband while achieving a defined level of attenuation above the cut-off.

Another type of lowpass filter is the Chebyshev filter, which allows for a sharper roll-off at the expense of passband ripple [30]. This filter is suitable when a steeper cutoff is required.

2.7 Diffusors

This chapter will delve into the concept of diffusors, which play a crucial role in room acoustics by scattering sound energy and enhancing the spatial qualities of an environment. Diffusors are essential components in the design of concert halls, recording studios, home theaters, and other spaces where acoustic quality is of paramount importance. In many older buildings and concert halls, natural diffusors such as pillars, statues, and other objects are exhibited.

This chapter provides an overview of diffusors, focusing on the theory behind the chosen diffusor type used for the modules created.

2.7.1 QRD Diffusors

QRD diffusors are widely used in room acoustics due to their effectiveness in scattering sound energy over a wide range of frequencies [31, 7]. The concept behind QRD diffursors is based on the mathematical properties of quadratic residues, which provides a pseudodorandom pattern of phase shifts and reflections [32]. By employing a periodic arrangement of wells and ridges with varying depths, QRD diffusors disperse incident sound waves in a controlled manner, reducing flutter echoes and enhancing spatial diffusion.

2.7.1.1 Design Principles for a QRD Diffusor

Designing QRD diffusors involves determining the depth and width of wells and ridges to achieve desired diffusion characteristics across the frequency spectrum of interest [31]. Scattering coefficients quantify the ability of a diffusor to scatter sound energy in different directions, while diffusion coefficients measure the overall scattering efficiency. Additionally, understanding the angular response of the diffusor, which characterizes its performance at different incident angles, is crucial for achieving uniform diffusion throughout the listening area.

A QRD diffusor is constructed as a periodic structure with changing depths and the same width for all elements. Each period is symmetrical with the length of N number of elements, where N is a prime number. Two methods of constructing the wells exist: one involves separating each element with a thin wall, and the other method omits this thin wall between each well [33]. The depth of each element in the periodic QRD diffusors are based on a series that emerge by dividing a quadratic number by a prime number. It is given as

$$n = \text{remainder}\left(\frac{m^2}{N}\right) = m^2 - N \cdot \text{integer}\left(\frac{m^2}{N}\right), \quad m \in \mathbb{N} \tag{2.11}$$

In the given equation, N represents the number of elements in the periodic series, which is a prime number larger than 2. m corresponds to the element number in the periodic series, and n is a discrete number describing the depth of each element [33]. The number series of n will consist of values between 0 and $n_{max} < N$, and the real depth value, d, of each element is given as

$$d = \frac{d_{\max} \cdot n}{n_{\max}} \tag{2.12}$$

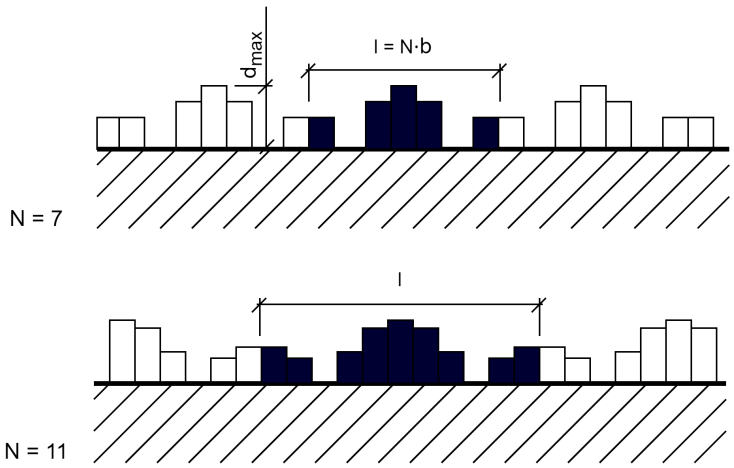

Figure 2.7.1: Structure for two different QRD-diffusors with length $N = 7$ and $N = 11$. The series is marked by the black boxes and the repetitive series is marked as transparent boxes. The discrete depth n of each series is listed in Table 2.7.1.

Table 2.7.1: Example of number series of n in a QRD-diffusor. For every type of diffusor the first symmetric half of a series is marked in bold numbers.

Type of QRD-Diffusor	n_{max}	element number m														
		0	1	2	3	4	5	6	7	8	9	10	11	12	13	14
N = 7	4	**0**	**1**	**4**	**2**	2	4	1	0	1	4	2	2	4	1	0
N = 11	9	**0**	**1**	**4**	**9**	**5**	3	3	5	9	4	1	0	1	4	9

Here, $d_{\max}$ is the depth of the deepest well in the QRD, n_{max} is the highest discrete depth value in the periodic series given by Equation (2.11). An example of two different QRD profiles can be seen in Figure 2.7.1 with the related values of n for the two cases shown in Table 2.7.1.

2.7.1.2 Frequency Range of a QRD-Diffusor

The frequency range of a QRD-diffusor is given by the different size parameters of the QRD such as well depth, N and the width of each well. In the context of QRD diffusers, three parameters are relevant to address the frequency range: f_0, f_{lower}, and f_{upper}. When considering various values of N with a consistent maximum well depth d_{max} and constant total length of the QRD, l, the upper frequency bound f_{upper} increase with an increase of N. This is because the upper bounds are primarily determined by the width of each well as seen in Equation (2.14), where b is the width of each well, c is the speed of sound in the propagating medium and λ_{upper} is the wavelength of the upper frequency. Theoretical upper bounds for high efficiency of sound scattering is the frequency where the width of each well is half the wavelength. The lower frequency bound, f_{lower}, is determined by the total length of the period of the QRD, l, and should have that each period is equal, or larger, than the wavelength of the lowest frequency of interest. The lower bounds should also be about an octave below the dimensional frequency f_0.

The equation including the two arguments for the lower frequency bound is seen in Equation (2.15)

$$f_0 = \frac{172 \cdot n_{\max}}{N \cdot d_{\max}} \tag{2.13}$$

$$f_{upper} \approx \frac{2c}{\lambda_{upper}} = \frac{c}{2 \cdot b} \tag{2.14}$$

$$\begin{aligned} f_{lower} &\approx \frac{c}{l} \\ f_{lower} &\approx 0.5 \cdot f_0 \end{aligned} \tag{2.15}$$

2.8 Transmission line matrix

The Transmission Line Matrix (TLM) method, rooted in the principles established by Dutch scientist Huygens [34], offers an unique approach to wave propagation simulations. Huygens conceptualized wave propagation as a series of elastic collisions between molecules, accurately capturing the physical essence of acoustic waves traveling through a medium enveloped by an electromechanical field. Building upon this notion, Peter Johns developed the concept of using Huygens' principle to compute the wave equation, leading to the inception of the Transmission Line Matrix (TLM) approach [35]. The TLM framework resembles an interconnected matrix grid, analogous to an analog circuit.

Sound wave propagation and radiation problems necessitate solving the wave equation in the time domain or the Helmholtz equation in the frequency domain, subject to appropriate boundary conditions. Analytical solutions are often unattainable due to the complexity of general boundary shapes and conditions. Consequently, numerical methods such as finite difference (FD), finite element (FEM), and boundary element methods (BEM) are employed to solve the governing differential equations numerically [36, 37, 38].

Alternatively, a physical modeling approach offers an alternative simulation methodology in which the phenomenon is authentically traced. The discrete Huygens model aligns well with this approach, as Huygens postulated that a wavefront comprises secondary radiators that generate spherical wavelets, culminating in the formation of a new spherical wavefront. By repeating this mechanism, Huygens elucidated the cause of wave propagation.

The TLM method, as a time-domain approach, encapsulates a simple yet powerful idea, providing an effective means of modeling wave propagation.

A 2D scenario without loss of generality can be seen in Figure 2.8.1. At time-step $n = 1$, an incoming pulse with a value of 1 enters a node. In the subsequent time-step $n = 2$, the wave propagates to all neighboring branches, resulting in a negative pulse being reflected back into the branch it originated from to satisfy the law of conservation of energy. During the third time-step, each reflected pulse generates additional scattering pulses in all interconnected branches associated with the given node. This iterative process continues throughout the finite duration of the simulation. When a wave pulse reaches a junction within the system, its behavior is determined by a local rule. This rule governs the reflection and

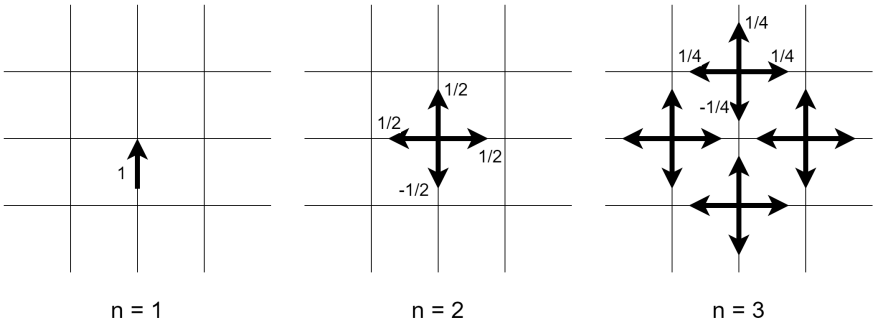

Figure 2.8.1: TLM basics for three consecutive time steps of n in a 2D case. The left most figure show $n = 1$ and an incident pulse is entering a node. The middle figure show the following time step and the scattering pulses. The right most figure show the spreading of pulses after a total of 3 time steps.

transmission of the pulse and is derived by evaluating the plane wave reflection coefficient at an impedance discontinuity while adhering to the principle of energy conservation [39].

2.8.1 Incident and Scattering Pulses on a Grid Node

In the context of examining various potential incidences at a specific junction denoted by a row, column and depth index (i, j, k) of a 3D TLM mesh, it is possible to construct a scattering matrix. This matrix relates the incident waves at time t to the resulting waves in the six channels connected to that particular point at time $t + \Delta t$. In the case of a three-dimensional scenario, the scattering matrix can be represented as follows[34]:

$$
{}_{t+\Delta t}\begin{bmatrix} R^w \\ R^n \\ R^s \\ R^e \\ R^u \\ R^d \end{bmatrix}_{i,j,k} = \frac{1}{3} \begin{bmatrix} -2 & 1 & 1 & 1 & 1 & 1 \\ 1 & -2 & 1 & 1 & 1 & 1 \\ 1 & 1 & -2 & 1 & 1 & 1 \\ 1 & 1 & 1 & -2 & 1 & 1 \\ 1 & 1 & 1 & 1 & -2 & 1 \\ 1 & 1 & 1 & 1 & 1 & -2 \end{bmatrix} \cdot \begin{bmatrix} I^w \\ I^n \\ I^s \\ I^e \\ I^u \\ I^d \end{bmatrix}_{i,j,k} \tag{2.16}
$$

The symbols in the above equation are defined as follows: R represents the reflected pulses, I represents the incident pulses, and the superscripts w, n, e, s, u, and d correspond to the cardinal directions West, North, East, South, Up, and Down, respectively.

In the context of each individual node, the overall pressure is determined by evaluating the following expression:

$$
P_{i,j,k} = \frac{1}{3}\left(I^w + I^n + I^e + I^s + I^u + I^d\right) \tag{2.17}
$$

The pulses that are dispersed propagate through the branches in opposite directions. When the field is partitioned into square meshes, the dispersed pulses transform into incoming pulses for the neighboring elements, where scattering occurs once more. The incoming pulses at a node located at position (i, j, k) are indicated by the dispersed pulses at the adjacent nodes.

$$
\begin{aligned}
{}_{n+1}I^{n}_{i,j,k} &= {}_{n+1}R^{s}_{i-1,j,k}, & {}_{n+1}I^{s}_{i,j,k} &= {}_{n+1}R^{n}_{i+1,j,k} \\
{}_{n+1}I^{w}_{i,j,k} &= {}_{n+1}R^{e}_{i,j-1,k}, & {}_{n+1}I^{w}_{i,j,k} &= {}_{n+1}R^{e}_{i,j+1,k} \\
{}_{n+1}I^{u}_{i,j,k} &= {}_{n+1}R^{d}_{i-1,j,k}, & {}_{n+1}I^{u}_{i,j,k} &= {}_{n+1}R^{d}_{i+1,j,k}
\end{aligned}
\tag{2.18}
$$

By applying Equations (2.16)-(2.18) to each node in a repetitive manner, it becomes possible to track the field's impulse response over consecutive time intervals. This approach inherently operates in the time domain, making it highly advantageous for simulating and visualizing wave behavior on a computer system. Furthermore, this method offers valuable insights into the dynamic characteristics of the wave phenomena being studied.

2.8.2 Boundary Conditions

The following section examines the boundary conditions to be imposed on the TLM grid. Specifically, examination of scenarios involving a rigid wall and a sound-absorbing wall. In TLM modeling, these boundaries are typically positioned between two nodes or at the furthest end of the element's branch arms. To incorporate these boundaries, a reflection coefficient R is introduced.

For instance, if the branch extending westward from a particular node encounters a rigid wall, the reflection coefficient R is set to 1. This condition can be applied to any branch by utilizing the following relation:

$$
{}_{n}I^{\text{branch}}_{i,j,k} = {}_{n}R^{\text{branch}}_{i,j,k}, \quad \text{branch} \in \{w, n, e, s, u, d\} \tag{2.19}
$$

In this context, the variable *branch* serves as a temporary indicator representing one of the six potential branches connected to a given node, while n represents the specific time-step value. When it comes to the sound-absorbing wall, the boundary is concluded with a resisting load denoted as Z_a. The reflection coefficient is defined as follows[34]:

$$
R = \frac{Z_a - Z_0}{Z_a + Z_0} \tag{2.20}
$$

Here, the characteristic impedance of the branch or the surrounding medium is represented as Z_0. It's important to note that the reflection coefficient R mentioned is distinct from the reflection coefficient associated with a wave reflecting at the TLM network's wall, where the sound speed differs from that within a branch [34]. Instead, the reflection coefficient Γ is defined as follows:

$$
\Gamma = \frac{Z_a - Z_T}{Z_a + Z_T} \tag{2.21}
$$

In this context, Z_T represents the characteristic impedance associated with the propagation of sound within the network. By combining Equations (2.20) and (2.21), we establish the relationship between R and Γ as follows:

$$
R = \frac{(1+\Gamma) - \sqrt{2}\,(1-\Gamma)}{(1+\Gamma) + \sqrt{2}\,(1-\Gamma)} \tag{2.22}
$$

In order to incorporate the reflection coefficient into a branch during the propagation process, the value of R derived from Equation 2.22 is multiplied by the reflected pulse as defined in Equation (2.16). In the case where a branch encounters a non-reflective boundary with Γ set to 0, simulating a free-field environment, the expression for R is simplified to:

$$R = \frac{1-\sqrt{2}}{1+\sqrt{2}} \approx -0.17 \tag{2.23}$$

This thesis does not consider cases involving waves striking the boundary at arbitrary angles. However, if the propagation process requires treatments for such scenarios, the work by Juan A. Morente et al. titled "Absorbing Boundary Conditions for the TLM Method" [40] provides relevant literature on the process.

2.8.3 Speed of Waves inside TLM

In the TLM method, the speed of sound is proportional to the speed of sound in free space by the factor $1/\sqrt{2}$, as seen in Equation (2.24). This variation arises due to the discrete nature of the TLM technique. The time step in the TLM method is typically set to maintain numerical stability, which introduces the factor in the propagation speed [34]. In contrast, the real speed of sound is continuous and follows the well known value at a specific medium, depending on factors like temperature, pressure and the mediums properties. In the discrete TLM grid, the speed of sound is constrained by the grid resolution and the numerical time step, leading to the $1/\sqrt{2}$ proportionality factor.

$$c_T = \frac{1}{\sqrt{2}} c_0 \tag{2.24}$$

Here, c_T is the speed of sound in the TLM grid, and c_0 is the speed of sound in free space.

2.9 Programming Language Julia

Julia is an open-source, high-level programming language released in 2012, offering significant speed advantages in handling "for" loops compared to languages like Python. This chapter delves into the underlying reasons for Julia's efficiency and its superiority in the context of this thesis.

2.9.1 Julia's Compilation Approach

Julia utilizes a just-in-time (JIT) compilation approach, combining the flexibility of an interpreted language with the speed of a compiled language. During runtime, Julia dynamically compiles the loop code, generating optimized machine code tailored to the specific problem. This dynamic compilation eliminates the need for manual optimizations and allows Julia to execute loops efficiently without sacrificing performance [41].

2.9.2 Type-Systems and Multiple Dispatch

Julia's type system and multiple dispatch further contribute to its performance advantage. By leveraging multiple dispatches, Julia can specialize functions based on specific argument types, leading to more efficient code execution. This feature helps Julia avoid the overhead of dynamic dispatch, which is common in object-oriented languages like Python [42]. Additionally, Julia's ability to infer and utilize type information during compilation enables efficient memory access and eliminates unnecessary type-checking overhead [41].

2.9.3 Speed Advantage of Julia

Julia's compiled nature provides a clear speed advantage, particularly evident in for-loops. When iterating through a large number of calculations for a given dataset, Julia significantly outperforms Python, offering faster iteration times. Apart from Julia, there are alternative approaches to achieve similar advantages in loop performance, one of which is the use of Numba, a just-in-time (JIT) compiler for Python. Numba can accelerate Python functions by translating them into machine code using the LLVM compiler infrastructure. LLVM is a collection of modular and reusable compiler and toolchain technologies designed to optimize the compilation process and generate efficient machine code for a wide range of programming languages. It provides a framework for building compilers and code optimization tools that can target various platforms and architectures. By using Numba's JIT compilation, Python code can achieve significant speed improvements, especially in computationally intensive tasks involving for-loops and numerical computations [43].

2.10 Uncertainty

Uncertainty analysis plays a cruical role in scientific research and measurements, including the field of acoustics. This chapter focuses on the assessment and quantification of uncertainties, providing a comprehensive understanding of how uncertainty affect the experimental results and the reliability of conclusions. The sources of uncertainty, methods of uncertainty estimation, and their practical implications in acoustical experiments will be discussed in this chapter.

Uncertainties can arise from various sources in experimental measurements and data analysis. It is important to identify and evaluate these sources to understand their imact on the overall measurement accuracy. For instance, Bentley [44] defines the measurement error as the difference between the measurement value and the true value, and states that accuracy is the closeness of the measured value to the true value. The ISO standard 98-3:2008 [45] avoids using the terms "true value" and "error", instead presenting the same concepts by the use of the measured result and its evaluated uncertainty, where the particular quantity subject to measurement is known as the measurand.

Some common sources of uncertainty include:

- Random Errors: Random errors are inherent fluctuations in measurements caused by various factors, such as instrument limitations, environmental

conditions, or statistical variations. They result in differences in repeated measurements and can be characterized statistically.

- Systematic Errors: Systematic errors arise from biases or flaws in measurement systems, calibration procedures, or experimental design. They consistently shift measurements in a particular direction, leading to a systematic deviation from the true value. Identifying and minimizing systematic errors are critical for ensuring accurate measurements.

- Instrument Uncertainty: Instruments have inherent uncertainties associated with their measurement capabilities. These uncertainties may arise from instrument specifications and calibration procedures, as well as factors like drift or limited resolution. Manufacturers' specifications and calibration certificates provide valuable information for quantifying instrument uncertainties.

- Model Assumptions: In computational and modeling studies, uncertainties can arise from simplifying assumptions, approximations, or limitations of the mathematical models used. Understanding the uncertainty introduced by model assumptions is crucial for interpreting the results and accessing their reliability.

- Data Processing and Analysis: Uncertainty can also be introduced during data processing and analysis, which may involve data filtering, interpolation, or curve fitting. The choice of algorithms, assumptions, and statistical techniques can significantly impact the final uncertainty estimation.

Being able to quantify these uncertainties will help with data analysis and result in better presentation of results and its uncertainty.

2.10.1 Sample Mean and Standard Deviation

In statistical analysis, the sample mean and standard deviation are fundamental measures used to describe and summarize data, offering insights into the central tendency and dispersion of a sample. This chapter delves into the concepts of sample mean and standard deviation, along with their calculation methods.

The sample mean, denoted as $\bar{X}$, represents the arithmetic average of a set of observations. It provides an estimate of the population mean, which is the average value of the entire population from which a sample was drawn. The sample mean is calculated by summing all the individual values and dividing the sum by the sample size N [46], as seen in Equation (2.25). However, the sample mean is sensitive to extreme values, as it incorporates every observation in the sample.

$$\bar{X} = \frac{1}{N} \sum_{i=1}^{N} X_i \tag{2.25}$$

The standard deviation, denoted as S, quantifies the dispersion or variability of the data points around the sample mean. It provides a measure of the average distance between each data point and the mean. The sample standard deviation is calculated using Equation (2.26) [47].

$$S = \sqrt{\frac{\sum_{i=1}^{N} \left(X_i - \bar{X}\right)^2}{N-1}} \tag{2.26}$$

The sample standard deviation is essential for understanding the spread or scatter of data. It allows for comparisons of the variability between different datasets or groups. Higher standard deviation indicates a greater dispersion of values from the mean, while a lower standard deviation suggests a more tightly clustered dataset.

2.10.2 Absorption Coefficient Uncertainties related to ISO 354:2003

The uncertainty associated with the method of calculating the absorption coefficient following ISO 354:2003 arises from the measurement of reverberation times. This uncertainty becomes particularly significant when employing the interrupted noise method, where a noise signal is abruptly stopped, and the reverberation time is measured using decay curves. The relative standard deviation of the reverberation time T_{20}, is estimated as

$$\frac{\epsilon_{20}(T)}{T} = \sqrt{\frac{2.42 + \frac{3.59}{N}}{f \cdot T}} \tag{2.27}$$

The standard deviation of the reverberation time is represented as $\epsilon_{20}(T)$, where T denotes the measured reverberation time. Additionally, f stands for the center frequency of the one-third octave band, and N indicates the number of decay curves evaluated.

CHAPTER

THREE

METHODS

The methodology of this thesis consists of two main aspects: experimental measurements and simulations. Experimental measurements focused on the acoustical properties of the modules, with a specific emphasis on scattering and absorption. Simulations, on the other hand, primarily focused on the diffusive properties of the modules and served as validation for the simulation method employed.

The measurements were conducted in both an anechoic chamber and an reverberation chamber at the Faculty of Information Technology and Electrical Engineering (IE) at the Norwegian University of Science and Technology (NTNU). The objective of the measurements was to verify simulation results and identify the modules' strengths in terms of sound energy spreading and absorption qualities. Notably, all measured properties are expressed in relative units, eliminating the need for calibration for absolute measurements.

3.1 Construction of the Modules

The construction of the modules is a crucial aspect of this thesis. While the building process is exciting, detailed construction plans and sensitive information, such as specific location details and people involved, will not be disclosed. This decision is to respect privacy and maintain confidentiality.

The focus of this chapter remains on the overall methodology and key aspects of the module construction, ensuring that the theoretical and practical aspects are conveyed effectively without compromising sensitive information. By prioritizing privacy, the thesis maintains ethical standards and protects the interests of all parties involved in the project.

3.1.1 Sourcing Materials and the Focus on Recycling Materials

The construction took place at a private location, which also included all necessary tools for building the modules in a safe and efficient manner. The materials used was plywood for the modules walls, standard lumber for the QRD diffusor, piano hinges for fastening the bottom-part to the front-part of the modules, and ceiling tiles with an absorbtive function for the absorbers. Detailed list of materials and

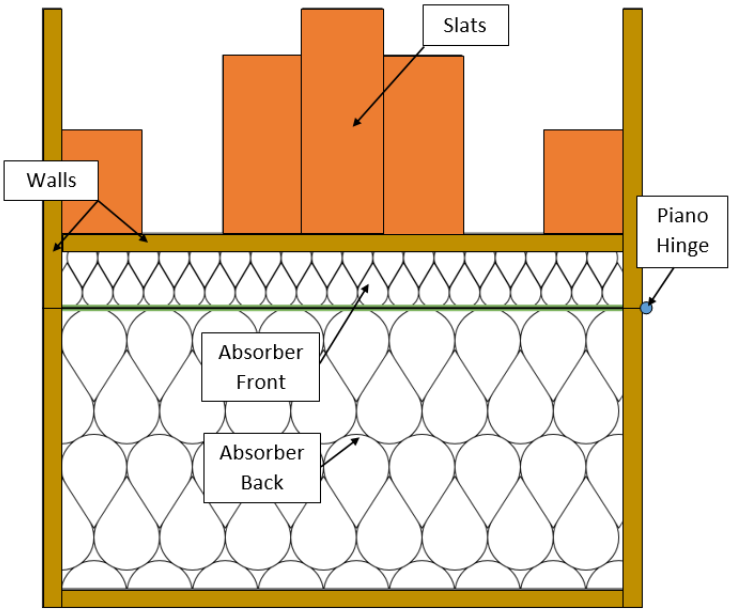

Figure 3.1.1: Cross section of the module.

the dimensions can be seen in Table 3.1.1 as well as a cross-section of the module in Figure 3.1.1.

This chapter focuses on the creation of modules with a strong emphasis on reusing/recycling materials. The motivation behind this approach lies in utilizing waste materials from construction sites or buildings destined for demolition. By repurposing these materials, interior pieces with acoustical functions can be crafted.

Sourcing these recycled materials can be uncertain, as they are often considered waste from construction processes, resulting from cutting elements to wrong lengths or materials not meeting engineering requirements. Therefore, locating suitable source materials for the project lacked guarantees, and some components had to be store-bought to ensure consistency.

However, absorbers used in the modules were repurposed from an abandoned building soon to be demolished. A total of 147 absorber panels were saved and incorporated into the seven modules created.

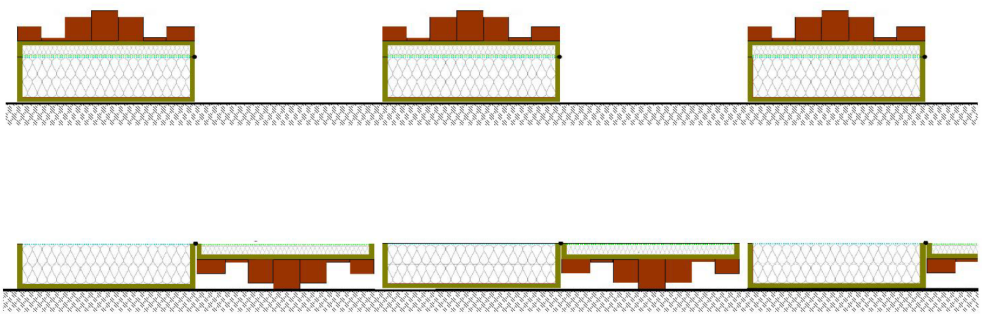

Figure 3.1.2: Top-most figure show the module in its "closed" state, while the bottom-most figure show the module in its "open" state.

Table 3.1.1: Materials used when creating the modules and its dimmension.

Name	Material	Dimension [mm]
Absorber Front	Ceiling tiles	1770x270x12
Absorber Back	Ceiling tiles	1770x270x104
Side walls	Plywood [Poppel]	1800x125x15
Backplate	Plywood [Poppel]	1770x270x15
Top-/bottom wall	Plywood [Poppel]	270x125x15
Slats - Big	Lumber [Pine]	1770x96x38
Slats - Medium	Lumber [Pine]	1770x74x38
Slats - Small	Lumber [Pine]	1770x49x38
Piano hinge	Brass	1800x25

The modules were purposefully designed with two distinct properties, offering both diffusive and absorptive capabilities, depending on their state. The states are categorized as "open" or "closed." In the "open" state, the module functions as an absorber, with an absorptive surface area of 1.07 m^2 for both the front and back parts, resulting in a total area of 2.14 m^2. Conversely, in the "closed" state, the front displays the QRD diffuser, allowing the module to function as a diffuser. Figure 3.1.2 showcases the modules in their two different states.

3.2 Measuring the Diffusive Properties

The diffusive properties of the QRD diffusor installed on each module will be evaluated according to the guidelines presented in ISO 17497-2:2012 [2]. This standard outlines a methodology for assessing the directional diffusion coefficient of surfaces within a free-field environment, utilizing an anechoic chamber. While ISO 17487-1 [48] introduces the concept of the random incidence scattering coefficient, the ISO 17497-2 standard focuses specifically on the diffusion coefficient. Unlike the scattering coefficient, which provides a general measurement of sound dispersion, the directional diffusion coefficient offers insights into the directional scattering behavior, thereby indicating the effectiveness of the diffusing surface. These coefficients serve distinct purposes and find relevance in different contexts.

Due to the physical constraints of the anechoic chamber and the optimal distances specified as per the standard, it is not feasible to achieve the recommended distances. As an alternative, three separate measurement series are conducted at different distances. This approach enables a comparative analysis and assessment of the QRD diffusor's diffusive properties within the given limitations.

3.2.1 Measurement Setup and Procedure

The measurements were conducted within an anechoic chamber located in room C138 at NTNU, Gløshaugen, Elektro D + B2. The anechoic chamber provides a controlled environment with minimal sound reflections, ensuring accurate measurements. It is constructed with sound-absorbing materials on the walls, ceiling,

and floor, predominantly using porous wedges [49, 50]. The anechoic chamber adheres to the qualifications outlined in ISO 3745 and ISO 261091 for assessing the degree of anechoic characteristics [51].

The measurement series were conducted with three distinct setups. The first two series utilized a microphone array shaped like a semicircle, as shown in Figure 3.2.1, with different radius values to maximize the utilization of the available room space. In the near-field measurement series, a radius of 1.1 m was employed. For the second series, a radius of 2.0 m was selected, optimizing the room's width without interference with the walls and absorbers. In the third series, the module was placed close to one of the corners, and measurements were taken for a quarter of a circle with a microphone array radius of 2.5 m, as depicted in Figure 3.2.2. Figure 3.2.1 and 3.2.2 illustrate the measurement setups, where the "module" box represents the object under test, the microphone semisphere/quartersphere indicates the intersected line between all microphone positions (ranging from -90 to 90 degrees around the module for the semisphere case and -90 to 0 degrees for the quarter of a circle case). It is of high importance that at least 80% of the microphone positions was outside the specular zone. The angular resolution between each microphone was set to 5°. The loudspeaker denotes the position of the sound source. These elements are positioned inside the anechoic chamber, while the control room outside the chamber houses the remaining tools and the computer running the EASERA software [19]. The EASERA software is connected to the sound card (Audio interface), which contains both the ADC and DAC. The signals from the DAC are fed back into the ADC as an electronic reference signal, used by EASERA to compute the impulse response. Additionally, the DAC signals are fed to a power amplifier to enhance the source signal delivered to the loudspeaker within the anechoic chamber.

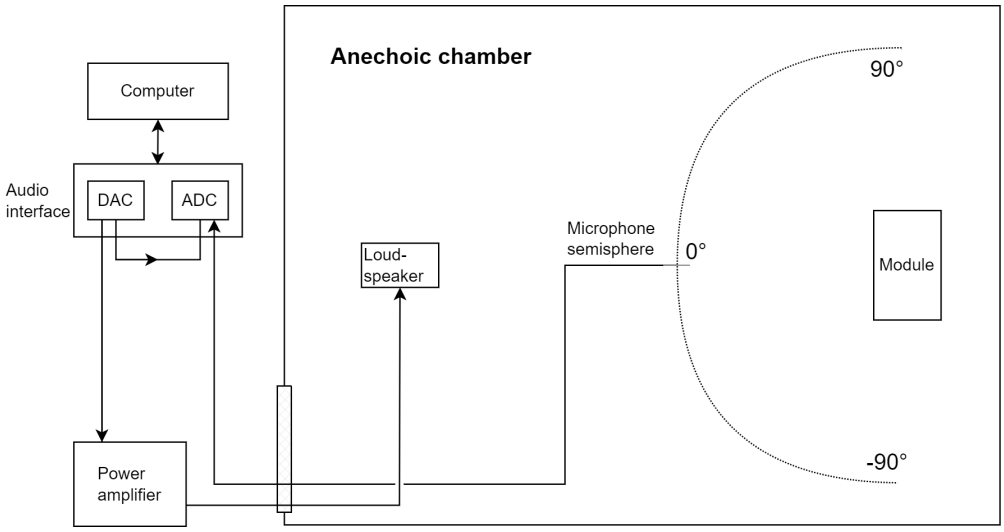

Figure 3.2.1: Illustration of the measurement setup related to the measurement procedure stated in ISO 17497-2:2012 [2] with the microphone array shaped as a semisphere.

In the first measurement series, the distance between the source and the module was set at 2.5 m. For the second and third series, a source distance of 4.6 m was utilized, representing the maximum achievable distance within the room without

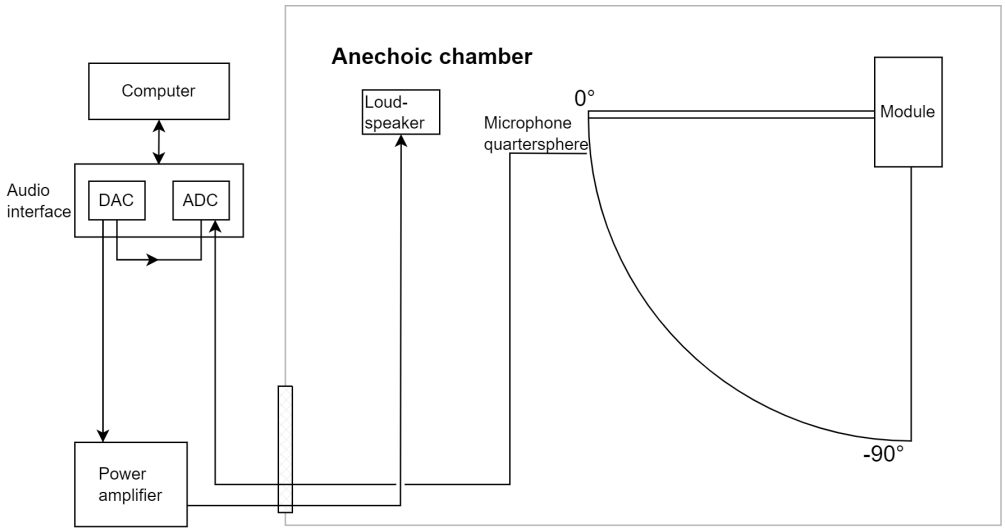

Figure 3.2.2: Illustration of the measurement setup related to the measurement procedure stated in ISO 17497-2:2012 [2] with the microphone array shaped as a quarter of a circle.

any interference with the room's walls.

The loudspeaker used in all three series was positioned at a distance from the module, aligned with the surface's normal direction, as seen in Figure 3.2.1 and 3.2.2. The loudspeaker was strategically placed to ensure that it illuminated the entire diffusor as if it were an omnidirectional source. The sound pressure distribution created by the loudspeaker aimed to match the expected characteristics of a true omnidirectional source, within ±2 dB in magnitude and ±20° in phase, over the reference flat surface. To maintain accurate measurements, the microphones employed possessed uniform sensitivity to all potential reflection paths from the diffusor to the microphone, within ±1 dB in magnitude and ±10° in phase.

All the equipment used for the measurements inside the anechoic chamber can be seen in Table 3.2.1.

Table 3.2.1: Equipment list for directional diffusion coefficient measurements performed on a custom diffusor in the anechoic chamber.

Equipment	Model number/type	Serial number
Recording software	EASERA 1.2.16.4 [19]	
Program for post-processing	Python [42]	
Loudspeaker	Tube speaker Given at Acosutic lab	
Microphone	NTI Audio M4261	3414
Sound card	ASIO Lynx Aurora USB	
Power amplifier	Rotel RB-1552 MKII	
Thermometer/hygrometer	CMOSens SHT1x (RH/T)	
Various cables and tape	N/A	
custom QRD diffusor with N=7	Plywood	

3.2.2 Measurements for Three Different Distance Values

Using EASERA software [19], a real-time analyzer for sound recording, a weighted logarithmic sweep was emitted from the loudspeaker inside the anechoic chamber. The sweep ranged from 100 Hz to 15 kHz and lasted for a duration of 5.6 seconds. EASERA processed the captured data and returned the impulse response measured by the microphone at every designated position. This measurement procedure was repeated for all microphone positions across the three measurement series. Both with and without the module in place, measurements were conducted at each microphone position. The measurement without the module served as a reference for data processing.

The data was then processed according to the guidelines outlined in ISO 17497-2:2012. While a detailed discussion of the standard is beyond the scope of this thesis, the key points will be highlighted.

In the initial phase, the earliest arrival time of reflections from the module was determined either by manually calculating the propagation time from the sound source as it left the source, interacted with the module, and was recorded at the microphone, or by inspecting the impulse response with and without the module present to identify the time when reflections were detected. The calculation or visual inspection of the impulse response helped identify signals exclusively associated with reflections from the module from the intial wave, to the last reflection off the module. However, the final reflections from the module posed challenges for manual calculation due to multiple diffractions by the module. As a result, visual inspection of the impulse response proved to be the most reliable method for determining the endpoint of the module's reflections.

3.3 Measuring the Absorption Coefficient

ISO 354:2003 is an internationally recognized standard that outlines precise methodologies for evaluating the sound absorption properties of materials within reverberation rooms [1]. This chapter focuses on providing a comprehensive setup procedure to replicate the conducted measurements accurately. The setup entails meticulous placement of microphones and objects within the reverberation room, ensuring the reliability and precision of sound absorption measurements. The standard specifies two distinct measurement procedures based on whether the material under test comprises a set of identical objects or a single object with a known surface area. Given that the modules in question possess a surface area of only 1.08 m^2 and can be arranged side by side, both procedures will be employed and subsequently compared for their efficacy and consistency.

3.3.1 Setup

The measurement equipment employed in this series is detailed in Table 3.3.1. The measurements were conducted within a reverberation room situated in room D0016 at NTNU, Gløshaugen, Elektro D+B2. The dimensions of the room measured 8.5 m in length, 6.0 m in width, and 5.2 m in height, resulting in a room volume of 265.2 m^3. These dimensions satisfy the requirement specified in the ISO 354:2003 standard, which mandates a minimum reverberation room volume of 150

m^3. Various objects were present within the room, including plastic screens that contributed to diffusing the sound field, stairs, platforms, trolleys, and miscellaneous unidentified objects. While these objects had no impact on the measurements, they remained in their respective positions throughout all measurement series.

Table 3.3.1: Equipment list for absorption coefficient measurement performed on the modules inside the reverberation chamber.

Equipment	Model number/type	Serial number
Recording Software	EASERA 1.2.16.4 [19]	
Program for Post-Processing	Python [42]	
Loudspeaker	Given at Acosutic lab	
Pressure Microphone	Norsonic Type 1201/30490	1837407
Pre-Amplifier	Bruel&Kjaer Type 1708	100407
Sound Card	Roland Studio-Capture	
Stereo Power Amplifier	NAD Electronics LTD Model 208	
Thermometer/hygrometer	CMOSens SHT1x (RH/T)	
Microphone Cable	Norsonic Nor 1408A	
Various other cables and tape	N/A	
Custom Absorber	Ceiling Tiles - Modules	
Foam Windscreen for Microphone	N/A	

All seven modules were positioned and marked within the room at their designated locations for both measurement series. The modules were labeled with tape and assigned numbers to ensure consistency in case of any remeasurements due to complications. Once all module positions were marked, the boxes were temporarily removed from the room. Subsequently, each microphone position was chosen, marked with tapes, and maintained consistently throughout each measurement series. It is noteworthy that only one microphone was used for all measurements. To comply with the measurement requirements, each microphone position was positioned at least 1 m away from any object or wall, 2 m from any sound source and 1.5 m away from other microphone positions.

A minimum of 12 decay curves were measured, ensuring spatial independence, with at least three different microphone positions and two distinct speaker positions. Therefore, the total number of sound source positions multiplied by the number of microphone positions needed to be at least 12 to meet the measurement requirements. Since the room housed two custom, identical loudspeakers placed diagonally in opposite corners, one at the ceiling-wall corner and the other at the floor-wall corner, the number of required microphone positions was reduced to six.

To ensure precise measurements, a microphone stand with a fixed height was utilized, resulting in all microphone positions being at the same height. Each microphone was set at a height of 1.66 m above the ground. Detailed dimensions and distance values can be found in Table 3.3.2. Figure 3.3.1 illustrates the room layout for the test where the modules were treated as individual objects as well as a plane surface. The square with a cross inside represents the data processing

equipment's location within the room, while the adjacent stick-figure denotes the operator's position for each measurement. Due to the need for manual handling of instruments, an operator was present inside the room throughout the measurements. The real-time analysis was conducted using EASERA software, which was installed on a laptop situated on-site. The laptop was connected to a sound card, which facilitated amplification for both the speakers and the microphone. The loudspeakers were connected to the same mono output, ensuring equal signal transmission to both.

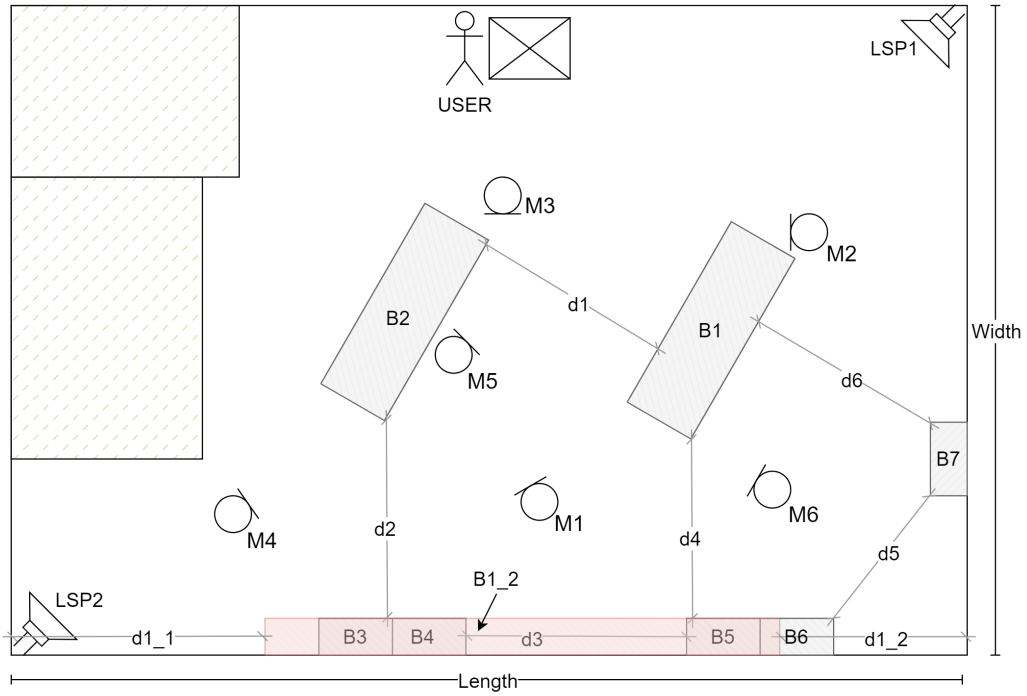

Figure 3.3.1: Reverberation Room Layout for ISO 354:2003 Measurements. Modules under test marked with gray boxes (denoted by the letter B and an enumerated number). Microphone positions indicated by microphone icons (denoted by the letter M followed by the position number). Plane absorber location highlighted in red (denoted as $B1\_2$).

3.3.2 Reference Measurements

To determine the absorption coefficient, a series of reference measurements was conducted using the interrupted noise method. This method involves filling the room with a significant amount of sound and then abruptly ending the noise, followed by measuring the decay of the sound at different microphone positions. To fulfill the requirement of a continuous frequency spectrum, each loudspeaker emitted broad-band noise. The duration of the noise emission was set to 20 seconds to ensure adequate room saturation before abruptly ceasing the sound and capturing the decay curves for all relevant third-octave bands.

The frequency range of interest is the third-octave bands from 100 Hz to 8 KHz. The noise source employed was white noise sampled at a rate of 48 KHz, as specified in the EASERA software.

Table 3.3.2: Distance values for the measurement series following ISO 354:2003. All distances are related to Figure 3.3.1.

Distance	Value	Unit
d1	2.1	m
d2	2.1	m
d3	2.85	m
d4	2.2	m
d5	2.05	m
d6	2.3	m
d1_2	2.25	m
d2_2	2.05	m

3.3.3 Measurements of a Plane Absorber

The seven modules were aligned against the wall, as shown in Figure 3.3.1. The plane absorber are denoted as $B1\_2$ and marked by a red box with diagonal fill. The total surface area of the modules is 7.56 m^2, with dimensions of 1.8x4.2 m. However, the required minimum distance of 0.75 m from any edge or wall of the room is neglected when placing the absorbers at the wall.

3.3.4 Measurements of a Specified Array of Test Objects

The modules were strategically positioned throughout the room to ensure that each object was at least 2 m apart from one another, adhering to the specified requirements. The arrangement of the modules can be observed in Figure 3.3.1, where they are indicated by gray boxes with diagonal fill, labeled as B1-B7. B1 and B2 were placed on the floor, while the remaining modules were positioned against the wall. This layout was chosen as the most optimal configuration, taking into consideration the fixed positioning of certain objects within the reverberation chamber.

3.3.5 Simplifications and Post Processing

Since the environmental conditions, such as relative humidity and temperature, in the test room is controlled during the measurements, no correction for the air attenuation has been applied. Due to this simplification, the absorption coefficient α_S has been evaluated following:

$$\alpha_S = \frac{55.3 \cdot V}{c \cdot S} \left(\frac{1}{T_2} - \frac{1}{T_1} \right) \tag{3.1}$$

V marks the volume of the reverberation room (m^2), S denotes the area of the test subject (m^2), c is the speed of sound in air (m/s) given in Equation (3.2) [52]. The temperature inside the room is marked as t, and the decay curves with and without the test subject is denoted, respectively, as T_2 and T_1.

$$c = 343.2 \cdot \sqrt{\frac{T}{293}} \tag{3.2}$$

In Equation (3.2), c marks the estimate of speed of sound in air, and T is the absolute temperature in Kelvin.

3.4 TLM model

The upcoming chapter provides an in-depth exploration of the procedures and techniques used to develop and simulate a Julia-based TLM model for investigating acoustic phenomena and testing the diffusive properties of the module. It covers the step-by-step construction of the TLM model, including the formulation of propagation formulas and grid setup. By elucidating implementation details and underlying principles, this chapter offers a comprehensive understanding of the methodology employed in simulating acoustic wave propagation using TLM.

While various approaches exist for implementing TLM models and propagation rules, this chapter focuses on explaining the methodology specifically applied in creating TLM models in Julia. It also showcase the set of propagation rules utilized and the optimizations employed to maximize the module's capabilities. The method implemented is based on Guillaume's approach, which utilizes different cases for propagation rules [53].

3.4.1 Creation of the TLM model and Labeled Array

The initialization process of the TLM grid in the proposed master thesis is founded upon a comprehensive set of user-defined parameters, aiming to tailor the simulated acoustic environment accurately. These parameters encompass essential variables such as the physical dimensions of the room, the desired sampling frequency, and the inter-node spacing within the TLM structure. Furthermore, the initialization incorporates influential factors like the ambient temperature, which modulates the speed of sound propagation within the medium, and the impedance value assigned to the acoustic medium. The user retains the flexibility to adjust these parameters, thereby facilitating the creation of an empty TLM grid alongside the requisite arrays, which form an integral part of the subsequent computational procedures.

In order to optimize control over each transmission line and enhance computational efficiency during the iterative process, the design of the TLM implementation in the master thesis incorporates an array-based approach. While a single 4D array could be employed to govern all nodes within the actual 3D space, along with the six associated transmission lines for each node, a more efficient scheme is adopted. This involves the creation of twelve distinct arrays, enabling individualized control over both incident and reflected pulses across the transmission lines. Specifically, for every transmission line, six arrays are allocated for manipulating the incident pulses, denoted as Ix, and an additional set of six arrays for managing the reflected pulses, designated as Rx. The subscript x corresponds to the specific direction of the transmission line emanating from each node, with N representing north, S representing south, and so forth. This segregated array structure ensures

Table 3.4.1: Propagation rules for the TLM matrix. Each node can have a subset of each of the given integer values giving each node the possibility of having up to 6 surrounding walls.

Value	Rule
Positive values	The medium in the given direction is of the sourrounding room
Negative values	The medium in the given direction is of the material under test
1	Different medium in the north direction
2	Objec in the south direction
3	Object in the west direction
4	Object in the east direction
5	Object in the down direction
6	Object in the up direction

fine-grained control over the propagation of incident and reflected pulses while optimizing computational performance during the iteration process.

Furthermore, two more arrays are created with the same size as the other twelve arrays. One for the overall pressure of each node in the grid, and one to hold all the propagation rules, called `'Labeled_tlm'`. The labeled TLM array is an array containing integer values that determine the propagation rule for each node in the grid. This array is directly overlayed to the TLM grid, and is a helpful tool when iterating over the grid. The set of rules used for the simulation can be seen in Table 3.4.1, and can easily be altered to contain more rules. Each element in the labeled tlm array contain a signed integer value, and is a set of the numbers 0,1,2,3,4,5 and 6, and it can contain a maximum of 1 of each of these numbers. The numbers decide which direction for each node an object, or a wall, is facing. If the number is 0, no object is in the nearby perimeter and all neighbouring nodes can be accessed, meaning there's no change in medium from the current node to any of its neighbours. In the propagation formula, when the value is greater than 0 (e.g., 145), specific rules are applied to account for the presence of an object, wall, or change in medium between the current node and the node in the given direction, (north, east, and down). On the other hand, if the value is less than 0 (e.g., -145), it signifies that the objects in the specified directions are off the diffusor, leading to an alteration in the reflection coefficient compared to the case with the value equal to 145. upon the activation of a rule, the propagation formula will determine the reflection factor and what will happen with the pulses for the given direction.

3.4.2 Simulation of Propagation Inside the TLM

The simulation process within the TLM framework revolves around discrete time steps, denoted by n, where the total simulation duration in seconds is divided into discrete intervals of length N. At each time step n, a series of calculations are performed for each node on the grid. The simulation process encompasses three main steps, but a flow diagram of the simulation process can be seen in

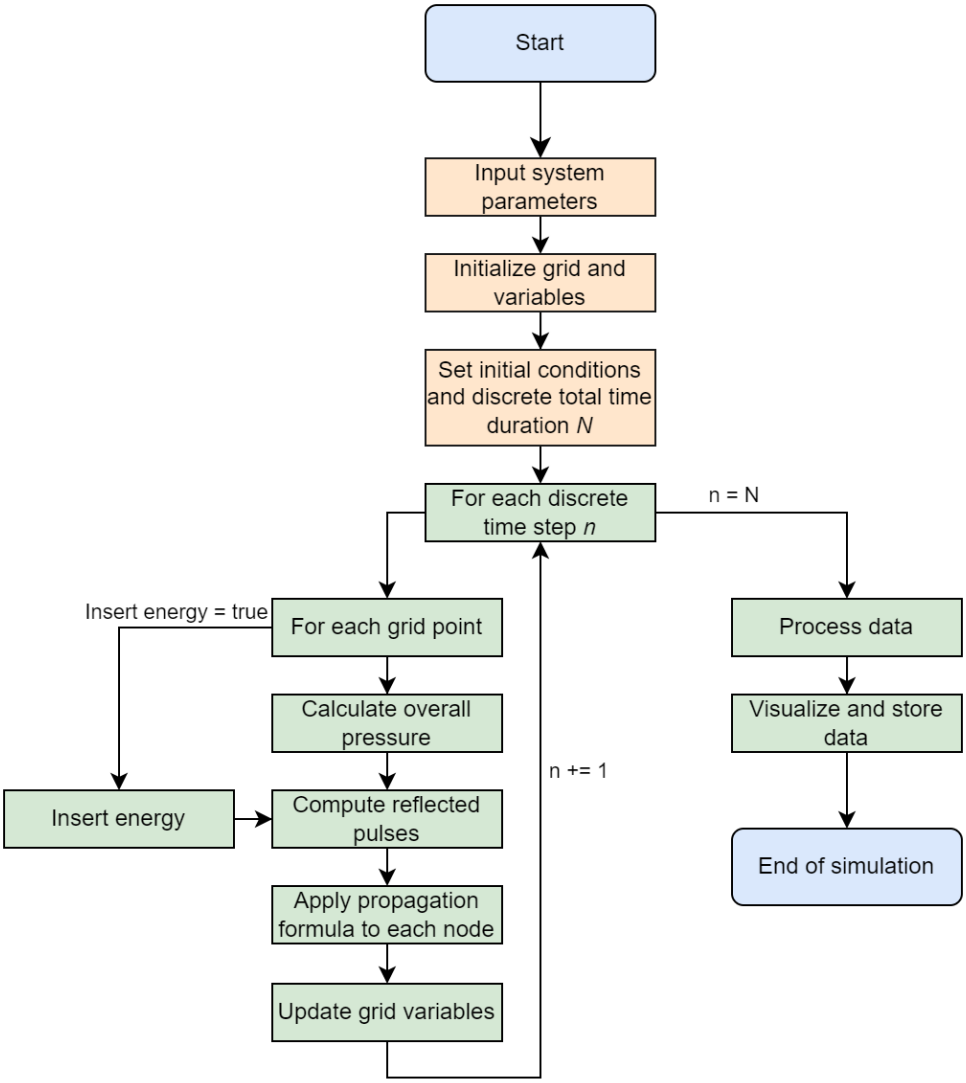

Figure 3.4.1: Flowchart of the simulation process in Julia. The blue boxes mark the endpoints of the simulation, the orange boxes mark initial setup and input parameters, and the green boxes mark the propagation and calculation steps.

Figure 3.4.1. Firstly, if specified, energy is inserted into the grid node. This allows the simulation of energy sources within the system. Second, the scattering pulses are computed using Equation (2.16). This step involves calculating the interaction and exchange of energy between neighbouring nodes. Lastly, the propagation rules, outlined in Table 3.4.1, are applied. In this thesis, a simplified set of propagation rules is utilized. The function iterates through each grid node and superimposes a labeled TLM array that specifies the propagation rule for that particular node.

The propagation function used in the simulation, which can be seen in the code snippet in Listing 1, employs a `'case()'` statement to retrieve the listed rules from the labeled TLM array. Additionally, a boolean variable `'Diffusor'`, is used to determine the appropriate reflection factor for the given node branch. When `'Diffusor'` is set to `'true'`, the grid interprets the presence of a diffusor medium in the corresponding direction of the node´s wall. If on the other hand `'Diffusor'` is set to `'false'`, the node interprets that the given branch is faced

```
function propagate()
    for i in 1:nx, j in 1:ny, k in 1:nz

        case_used, Diffusor = case(Labeled_tlm[i,j,k])
        for n in case_used
            if n==0 Refl=0 else Refl=Diffusor ? R[n+5] : R[n] end

            IN[i,j,k]=(1 in case_used) ? Refl*SN[i,j,k] : SS[i-1,j,k]
            IS[i,j,k]=(2 in case_used) ? Refl*SS[i,j,k] : SN[i+1,j,k]
            IW[i,j,k]=(3 in case_used) ? Refl*SW[i,j,k] : SE[i,j-1,k]
            IE[i,j,k]=(4 in case_used) ? Refl*SE[i,j,k] : SW[i,j+1,k]
            ID[i,j,k]=(5 in case_used) ? Refl*SD[i,j,k] : SU[i,j,k-1]
            IU[i,j,k]=(6 in case_used) ? Refl*SU[i,j,k] : SD[i,j,k+1]
        end
    end
    return
end
```

Listing 1: Propagation formula.

with the wall of the room. By specifying different rules and values to each branch, the reflection factor for the object a transmission line faces can easily be adjusted for the specific medium or object. For the simplified case used in this thesis, a total of twelve reflection values can be implemented, but can also be increased easily by just applying a larger set of rules. The next step in the propagation function is then to apply the correct propagation rule for the given branch.

3.4.3 Adding Objects Inside the TLM Model

The TLM model requires the inclusion of objects for measurement purposes. To facilitate this, a custom method was developed for inserting objects in the form of infinitely thin walls or planes into the model. This custom method involves a function that takes a two-dimensional array in the format ‘[[x_1,x_2],[y_1,y_2],[z_1,z_2]]’, where x, y, and z represent the real Cartesian coordinates, and the subscripts 1 and 2 indicate the start and end positions for the respective axis. This allows the creation of a plane in three-dimensional space.

However, the function has a limitation in that it only accepts planes where one of the axis values remains constant for both the start and end positions. It does not handle reflections at angles since all transmission lines exist only along the axis directions. To overcome this limitation, a method was applied to discretize diagonal planes into smaller straight lines, effectively pixelating the object. This process breaks the single diagonal line into multiple planes along the three Cartesian directions.

The function for inserting objects is closely related to the ‘`create_module_closed`’ function. This function takes several input parameters defining the module’s core dimensions, notably the starting point of the box and the desired rotation direction. it’s an one-dimensional list where each two-dimensional element array

represents each individual plane of the module. Subsequently, another function iterates through these arrays and updates the `'Labeled_tlm'` array with new labels before starting the simulation. This process enables easy insertion of objects into the grid for further analysis and measurements.

CHAPTER

FOUR

RESULTS

The results chapter aims to provide a comprehensive analysis of the simulations and measurements conducted in this study. It begins by presenting the theoretical frequency range of the module as a reference for comparing the simulation and measurement outcomes. Subsequently, the TLM simulation results and case studies will be presented and critically assessed, followed by the presentation of the measurement results. Finally, a comparison between the simulated values and the theoretical values will be presented. These findings serve the crucial purpose of validating the TLM model as a reliable simulation tool for the modules, especially when considering alterations to parameters in the development of new modules with varying specifications.

4.1 Module Parameters and Decisions

Table 4.1.1: Dimension values for the created modules.

Name	Value	Unit
Height	1800	mm
Width	300	mm
Depth - Front	125	mm
Depth - Back	125	mm
d_{max}	98	mm
width slats	38	mm
Wall thickness	15	mm
Absorber thickness Back	104	mm
Absorber thickness Front	12	mm

During the process of defining the module parameters, the primary focus was on determining the size and materials while ensuring that the functionality and frequency range of interest was effectively addressed. The optimized dimensions were chosen to be 1800 mm in length, 300 mm in width, and 250 mm in depth,

taking into consideration the materials used and the desired total weight of the module. This configuration resulted in an expected weight of 32 kg without absorbers and a total weight of 40 kg with absorbers. However, the measured total weight of the module was slightly higher, at 41.6 kg.

By setting the number of slats in the QRD to 7 ($N = 7$), the dimensional frequency f_0 was established at 1003 Hz, with upper and lower frequency bounds of 4513 Hz and 502 Hz, respectively. For detailed dimensions of the modules, refer to Table 4.1.1.

4.2 Validation of the TLM Model

The following chapter will outline the results gathered from the simulation process as well as the results from validating the TLM model.

4.2.1 Comparing the TLM model to Sabines Equation

To verify the implementation of the TLM model, a simulation was conducted using the parameters outlined below:

- Shoe-box shaped cavity with dimensions 4x3x2.5 m.
- Reflection coefficient Γ constant over all walls for three different values, case $\Gamma = 0.3$, $\Gamma = 0.5$ and $\Gamma = 0.8$.
- A source with a harmonic input signal set to 250 Hz driven for a total of 0.2 s.
- Mesh size $\Delta d = \frac{c}{fs}$, where fs is the sampling frequency set to 7 KHz.
- Computation of the Exponential Time-Weighted Sound Pressure Level, $L_{AF}(t)$ [1] for a given measurement node.
- Lowpass filtered using three different cut-off values, 300 Hz, $fs/10 = 700$ Hz and $fs/6 = 1167$ Hz.

For $\Gamma = 0.3$ (Figure 4.2.1), the four curves exhibit noticeable differences. Initially, all four graphs display similar decay for the first 55 dB after the source is turned off. However, the unfiltered decay curve starts to deviate from the remaining three curves. After an additional 20 dB drop, the orange curve (indicating the lowpass filtered decay curve with a cut-off at $fs/6$) starts to deviate from the blue (lowpass filtered with cut-off at $fs/10$) and black (lowpass filtered with cut-off at 300 Hz) curves. The orange graph then follows a shape similar to the unfiltered decay, but reduced by approximately 25 dB. After a total propagation time of 0.7 seconds, the blue graph starts to take on a shape similar to the orange and green graph, but with a much lower value of around -125 dB. The black curve reaches a minimum value after about 0.6 seconds, with a magnitude of -155 dB. The calculated reverberation time using Equation (2.4) is 0.09 s, and the simulated reverberation time, using the curve filtered at $fs/10$, is 0.08 s.

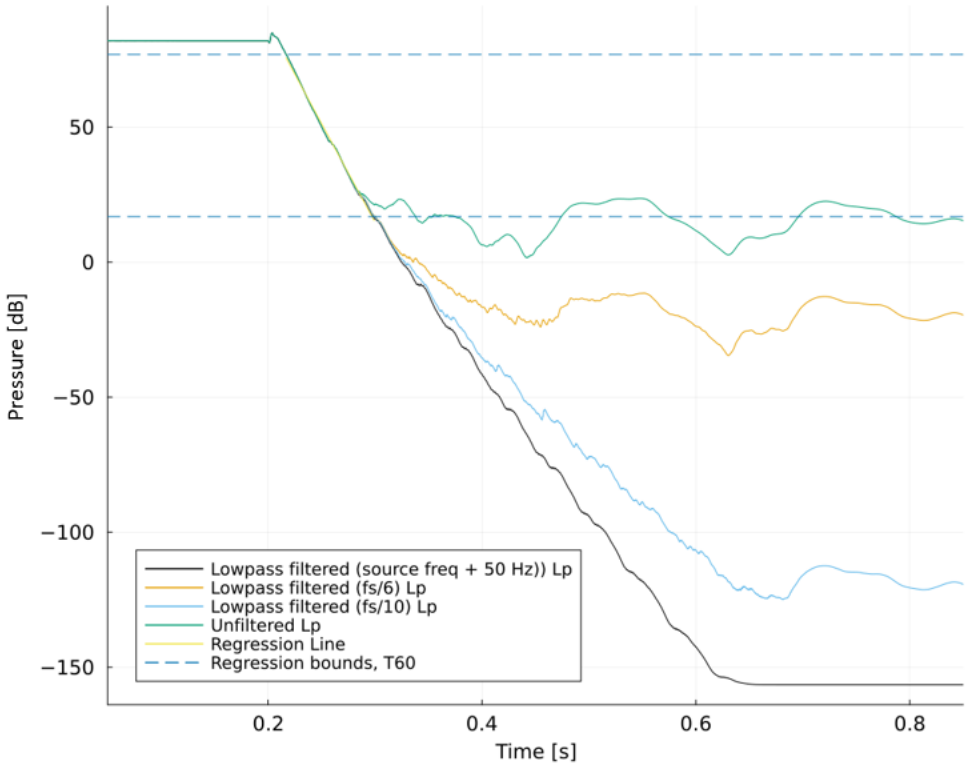

Figure 4.2.1: Decay Curves for a Simulation within the TLM Model. The Room Walls had a Reflection Coefficient of $\Gamma = 0.3$, and the Room Size was 4x3x2.5 m. The Regression Line Represents the $T60$ Line and is Based on the Lowpass Filtered Signal with Cutoff at $fs/10$.

In the figure, the regression bounds related to the 60 dB drop are depicted as blue dashed lines. Upon inspection of the unfiltered curve, it is evident that throughout the entire simulation period, the curve barely crosses this limit. This highlights the significance of filtering the measured data from the TLM grid. The curve exhibits signs of energy being trapped within the TLM grid, as it does not decrease its averaged energy but instead fluctuates around a constant value of 18 dB.

Similar observations are made for $\Gamma = 0.5$ (Figure 4.2.2), where all four graphs initially drop by 62 dB. Subsequently, they exhibit different decay rates, similar to the $\Gamma = 0.3$ case, except for the orange line. This time, the orange line deviates from the blue and black lines at an earlier stage than in the $\Gamma = 0.3$ case. For $\Gamma = 0.8$ (Figure 4.2.3), the separation is weaker, but after a 73 dB drop, the unfiltered signal begins to deviate from the remaining three curves.

Across all three cases, the unfiltered signal show signs of being independent of the reflection factor, especially for $\Gamma = 0.5$ and $\Gamma = 0.3$, remaining relatively equal throughout the duration after the source is turned off for both cases. Investigating the unfiltered decay from time 0.4 to 0.8 for both $\Gamma = 0.5$ and $\Gamma = 0.3$, the decay in both cases exhibits significant variations in strength, with differences in peak and nearby minimum values of over 20 dB. The unfiltered signal for all three cases show sign of not reducing the energy within the TLM, but rather fluctuate around a set pressure value. This convergence value the unfiltered decay seem to converge towards, is decreasing with the increase in reflection factor value. For $\Gamma = 0.3$

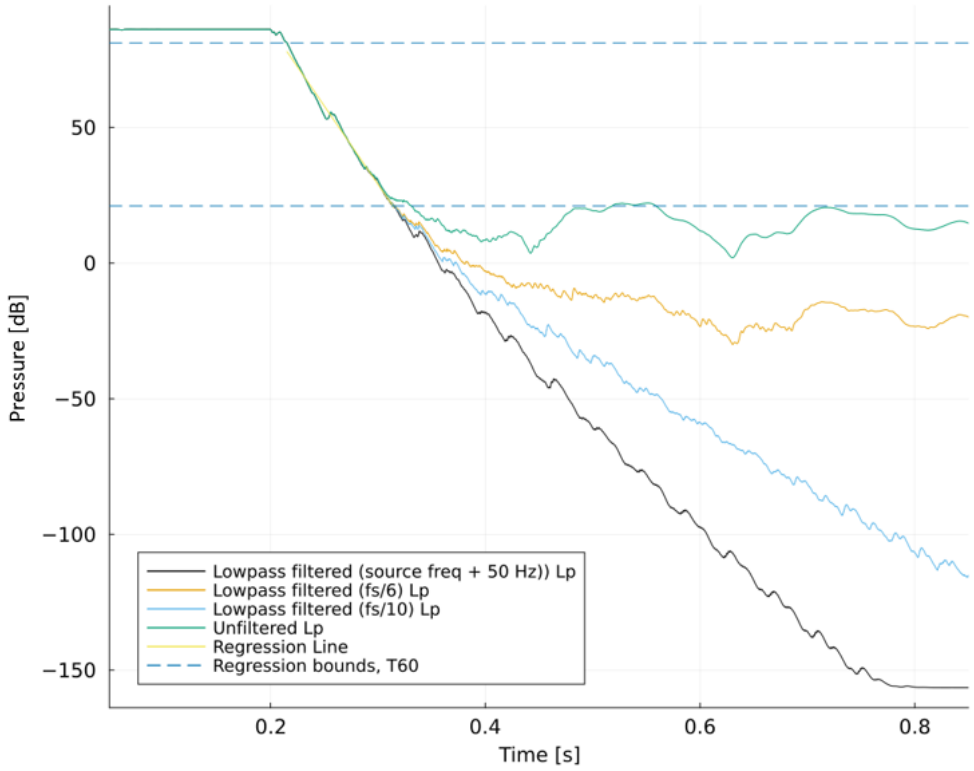

Figure 4.2.2: Decay Curves for a Simulation within the TLM Model. The Room Walls had a Reflection Coefficient of $\Gamma = 0.5$, and the Room Size was 4x3x2.5 m. The Regression Line Represents the $T60$ Line and is Based on the Lowpass Filtered Signal with Cut-off at $fs/10$.

this value is 18 dB, for $\Gamma = 0.5$ its 16 dB and for $\Gamma = 0.8$ its 8 dB. The decay time for the three cases are found in Table 4.2.1 together with results for reflection coefficients ranging from 0.1 to 0.9.

Nine simulated reverberation time calculations were performed for the same room, with only the reflection coefficient varying across the cases. The decay curves was filtered with a lowpass filter with cut-off at $fs/10$. The results, presented in Table 4.2.1, exhibit remarkable similarity to the theoretical values derived from Sabine's Equation, with discrepancies limited to a few percentage points. The average difference is computed as -2.47%, accompanied by a standard deviation of 6.30%. Rounding the reverberation times to two decimal places, the simulated values align closely with the theoretical values, calculated from Equation (2.4), within a range of ± 0.01 seconds. Notably, the accuracy of all simulated cases surpasses 90% concerning their alignment with the theoretical values.

A discernible trend emerges from the different values. For simulations characterized by $\Gamma < 0.7$, the differences remain consistently smaller than the corresponding theoretical values. Conversely, for cases with $\Gamma > 0.6$, the simulated results surpass the theoretical values. The pivotal turning point, transitioning from negative to positive differences, is observed slightly above $\Gamma = 0.6$. These findings signify the efficacy of the simulation approach and provide valuable insights into the impact of varying reflection coefficients on the reverberation time calculations.

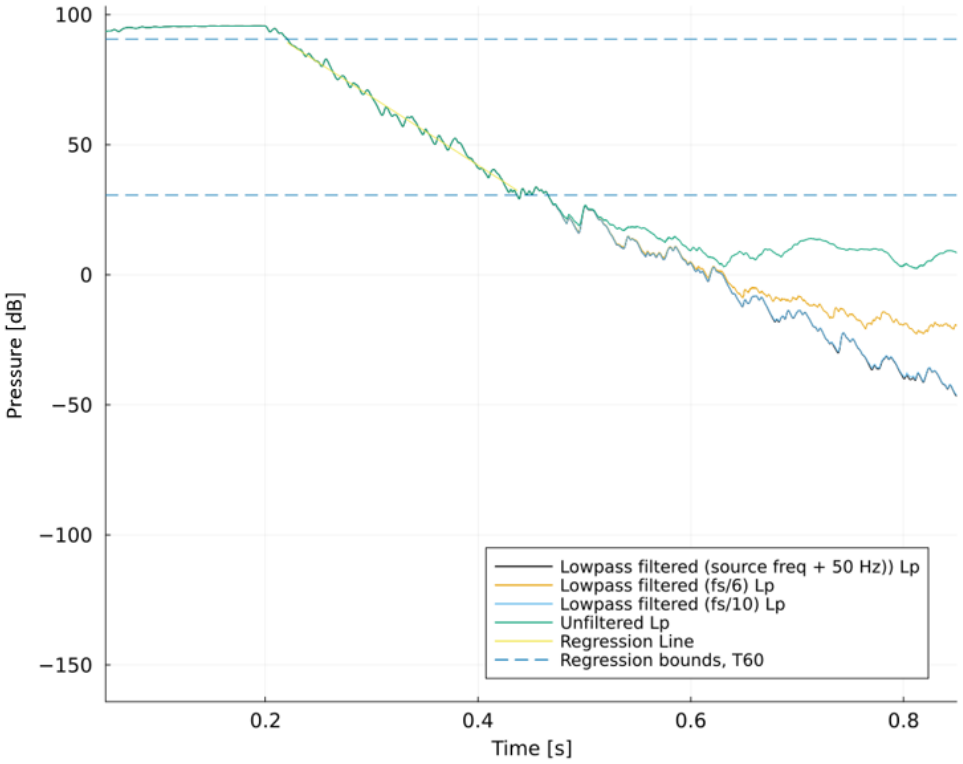

Figure 4.2.3: Decay Curves for a Simulation within the TLM Model. The Room Walls had a Reflection Coefficient of $\Gamma = 0.8$, and the Room Size was 4x3x2.5 m. The Regression Line Represents the $T60$ Line and is Based on the Lowpass Filtered Signal with Cut-off at $fs/10$.

Table 4.2.1: Comparison of Reverberation Time Calculated Using Sabine's Equation and Simulated $T60$ Values for Different Reflection Coefficients in a Room with Dimensions 4x3x2.5 m

Reflecton Coefficient Γ	D_R [s]	Simulated T60 [s]	Diffrence [%]
0.1	0.0821	0.0753	-8.3
0.2	0.0847	0.0768	-9.4
0.3	0.0894	0.0833	-6.8
0.4	0.0968	0.0899	-7.2
0.5	0.1084	0.1029	-5.1
0.6	0.1271	0.1266	-0.4
0.7	0.1595	0.1702	6.7
0.8	0.2259	0.2399	6.2
0.9	0.4281	0.4373	2.1

4.2.2 Propagation inside the TLM

This section presents the verification of propagation within the TLM, adhering to the prescribed rules. A heatmap of a TLM slice at a fixed height of 1.5 m showcases the propagation process with a short pulse and specific configurations. The sampling frequency is set at 65 KHz, resulting in a grid distance of $\Delta d = 5.27$ mm. The room dimensions are defined as 0.8x0.6x0.6 m, and the module is

positioned on the opposite side of the room to the source, facing the QRD towards the source. Inside the cavity, all walls have a reflection factor of 0, simulating a free-field environment, while the module has a reflection value of 1.

Figure 4.2.4 provides a visualization of the propagation process. Initially, an evident square wave formation of the wave is observed, gradually rounding off within a millisecond. Subsequently, a second wave closely follows the initial one which can be characterized as a ripple from the inserted wave. By 3.02 ms, the wave has reached the module and is diffracting along its sides. The presence of reflections and scattering off the box is visible, represented by a grayish color contrasting the surrounding medium. Moreover, within the deepest well, a stronger pressure value is distinctly apparent, indicated by a clear white color. Across all four slices, a distinct square pattern emerges, divided into smaller segments, with pulses propagating in all four directions. These findings demonstrate the fidelity of the TLM model in simulating sound propagation and provide valuable insights into the wave dynamics within the medium. The results reveal that the TLM method is based on a discrete set of directions, resulting in a blocky and pixelated propagation pattern, characterized by square-like propagation along its grid.

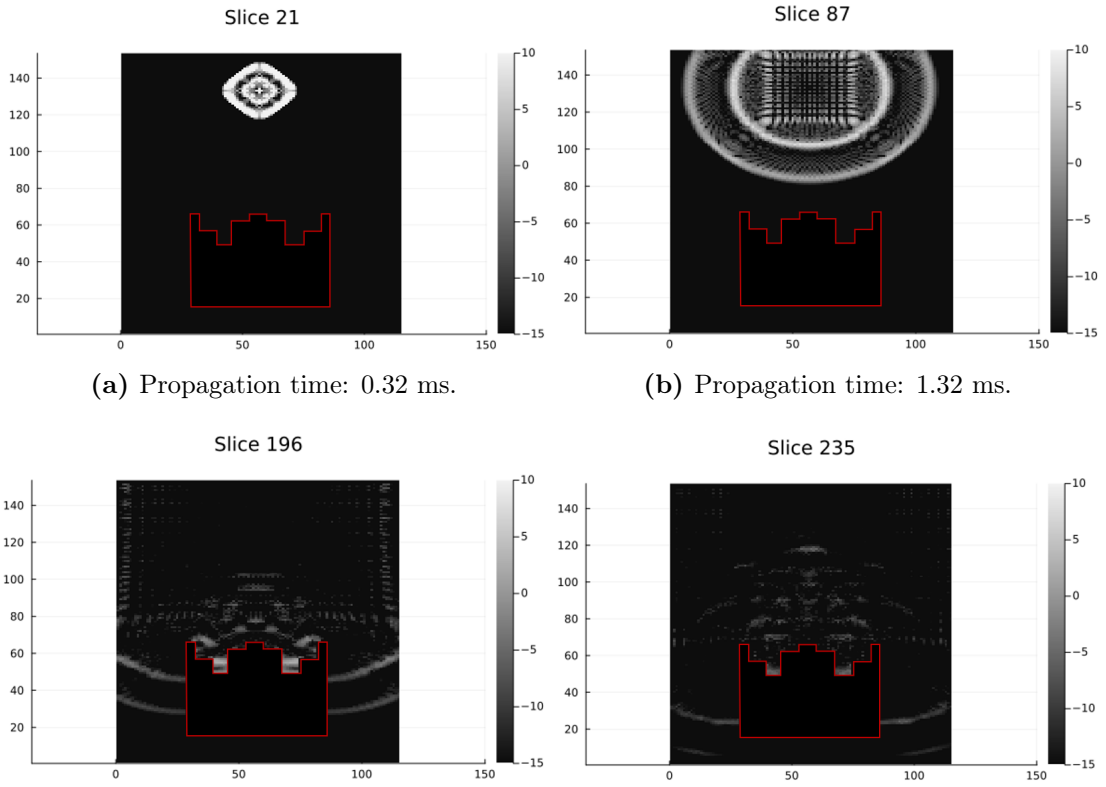

(a) Propagation time: 0.32 ms.

(b) Propagation time: 1.32 ms.

(c) Propagation time: 3.02 ms.

(d) Propagation time: 3.61 ms.

Figure 4.2.4: Propagation Inside a TLM Grid with Dimensions 0.8x0.6x0.6 m. The Grid's Sampling Frequency is 65 KHz, and the Module, Marked in Red, is Placed with a Reflection Coefficient Set to 1, while the Surrounding Walls are Set to 0, Simulating a Free-Field Environment.

4.2.3 Noise Inside the TLM

As seen from the decay curves with the different reflection coefficient values, the decay curve for the unfiltered signal show signs of being heavily affected by an internal noise. To further investigate this, a test for different sampling frequencies and room sizes were performed. A sweep signal was inserted into the room having free-field characteristics for a duration of 0.6 seconds, and then the sound pressure was measured for a total of 2 seconds after the noise sound source was finished, to measure any internal noise within the system. A total of four different cases were performed with two different sampling frequencies and two different room sizes. The cases are as follows:

- Case 1: $fs = 3500$ and room dimensions 4x3x2.5 m.
- Case 2: $fs = 1500$ and room dimensions 4x3x2.5 m.
- Case 3: $fs = 3500$ and room dimensions 8x6x5 m.
- Case 4: $fs = 1500$ and room dimensions 8x6x5 m.

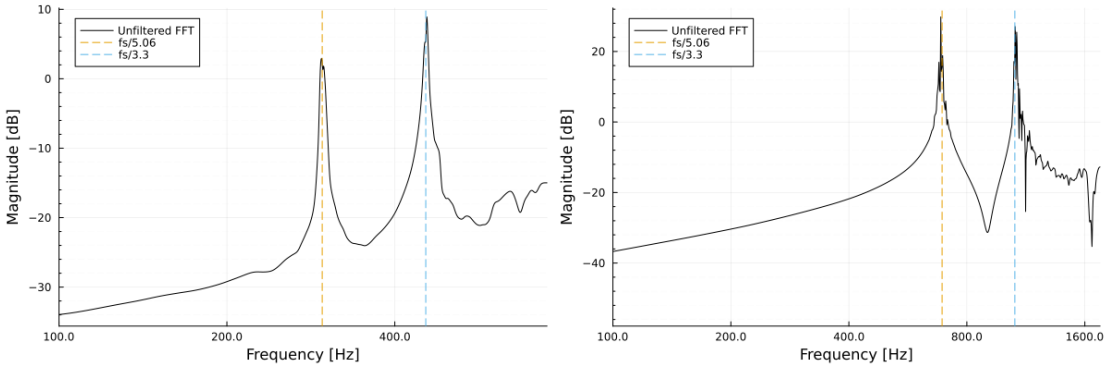

(a) **(b)**

Figure 4.2.5: Frequency response of internal noise measured within the TLM simulating a room of dimensions 4x3x2.5 m. (a) depicts the response for $fs = 1500$, and (b) displays the response for $fs = 3500$.

The frequency response for case 1 and 2 is visualised in Figure 4.2.5 and case 3 and 4 are displayed in Figure 4.2.6. As seen in the Figure 4.2.5, two distinct spikes is clearly visible for both frequency responses, but at different frequency values. The spikes, also marked by a red and blue dashed line, is exactly $fs/5.06$ and $fs/3$ in both cases. This is also the same for case 3 and 4, shown Figure 4.2.6, where the room size is doubled. This result identify that the internal noise within the TLM is affected only by the sampling frequency of the grid, without care for the size of the grid or reflection coefficients. The optimal upper frequency bound for a TLM grid is determined as $fs/10$, which is also supported by the frequency responses and the decay curves visualised previously, that clearly display a flatter frequency response for the frequencies below this limit, but remain strongly affected by noise for frequencies above this bound. For case 4, the frequency response show a very flat response for all frequencies below the $fs/10$ limit, and showcase the

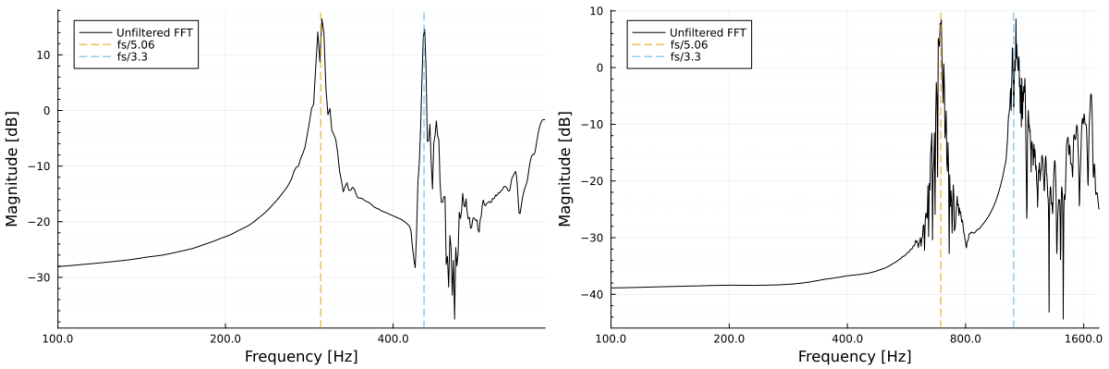

Figure 4.2.6: Frequency response of internal noise measured within the TLM simulating a room of dimensions 8x6x5 m. (a) depicts the response for $fs = 1500$, and (b) displays the response for $fs = 3500$.

importance of filtering the measured data. For cases 1, 2, and 3, the frequency response below the cut-off is not perfectly flat compared to the results from case 4. This discrepancy can be explained by considering the total number of grid points. In cases where the room size is large, a very high sampling frequency may not be necessary to achieve a flat response below the cut-off frequency. However, for smaller rooms, a higher sampling frequency is needed to achieve a flat response.

This observation is further supported by simulating the same room dimensions for cases 1 and 2 but increasing the sampling frequency to 6 KHz. The result, shown in Figure 4.2.7, indicates that for frequencies below 600 Hz, the response exhibits a particularly flat response compared to the results in case 1 and 2.

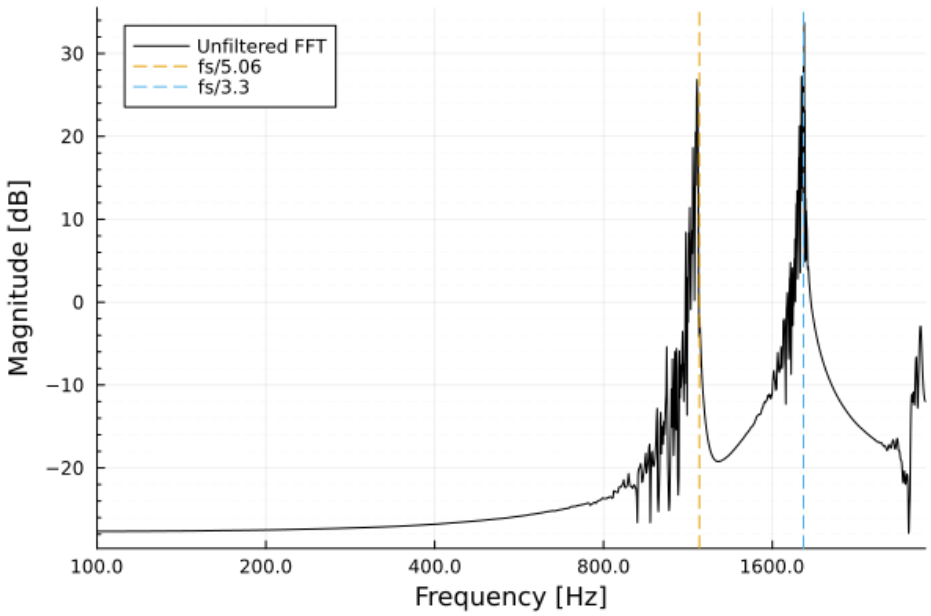

Figure 4.2.7: Frequency response of internal noise measured inside the TLM simulating a room of dimensions 4x3x2.5 m.

4.3 Simulating the Directional Diffusion Coefficient

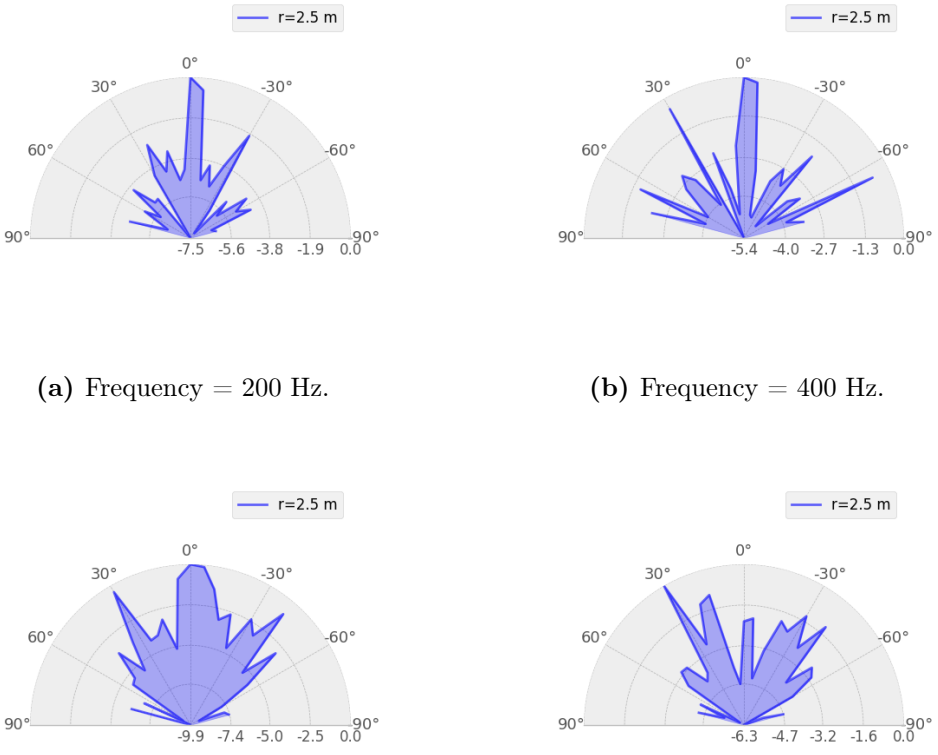

(a) Frequency = 200 Hz.

(b) Frequency = 400 Hz.

(c) Frequency = 800 Hz.

(d) Frequency = 1600 Hz.

Figure 4.3.1: Angular plots illustrating the directivity of the simulated module at a measuring distance of 2.5 m. The presented figures correspond to the octave bands ranging from 200 to 1600 Hz, labeled as (a)-(d). For additional third-octave plots covering the frequency range from 100 to 8000 Hz, please refer to Appendix E.

The simulation of the directional diffusion coefficient was carried out, employing distance values outlined in Chapter 3.2.2, which were matched to the third measurement series. However, to explore directional properties comprehensively, the microphone array was configured as a semicircle instead of a quadrant. The source signal comprised a sweep with a duration of 5.6 seconds, spanning frequencies from 100 Hz to 15 KHz. The impulse response for all microphone positions underwent identical data processing treatment as the real measurement series. Comprehensive angular plots illustrating the directivity of the simulated modules are provided in Appendix E. However, for focused analysis, specific angular plots illustrating the directivity for the modules are presented in Figure 4.3.1, spotlighting the directivity for octave bands from 200-1600 Hz.

Analyzing the plots for the 200 Hz case reveal a prominent lobe at 0°, flanked by side lobes at $-30°$ and $-60°$, as well as 25° and 50°, featuring smaller uneven peaks adjacent to the lobe peaks. Moving to the 400 Hz case, the main lobe

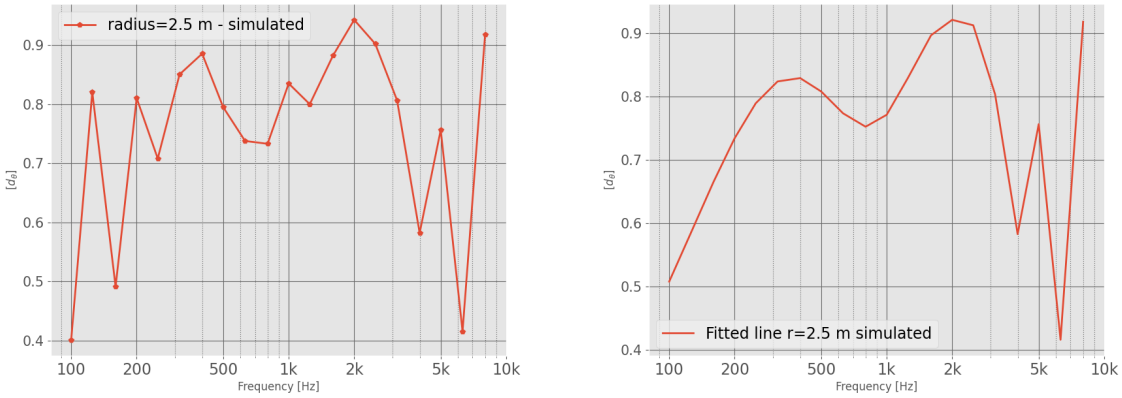

(a) Unfiltered

(b) Fitted polynomial line of order 10.

Figure 4.3.2: Directional diffusion coefficient (d_θ) as a function of frequency, depicted within the third-octave bands ranging from 100 to 8000 Hz. (a) show the unfiltered coefficient values and (b) display the polynomial fitted line of order 10, related to the results obtained from simulations adhering to the ISO 17497-2:2012 standard.

remains visible, but the side lobes become significantly thinner and harder to distinguish. Symmetry is apparent, with sidelobes observed at ±65° with smaller symmetry at ±30° due to the lobe at −30° is 2.5 dB weaker than the one at 30°. At 800 Hz, the main lobe widens compared to the previous frequencies, and sidelobes are noticeable around 30° and −40°. Furthermore, a third sidelobe is observed symmetrically around ±50°. At 1600 Hz, the strength of the main lobe exhibits weak intensity, dropping 2.2 dB lower than the sidelobe at 30°. Symmetrical sidelobes are observed at ±30°, and an additional lobe at 15° becomes distinguishable. Additionally, a third sidelobe is seen at ±50° with a value at -3 dB.

The computed directivity results were used to calculate the directional diffusion coefficient as a function of frequency and plotted in Figure 4.3.2. Remarkably high diffusion is observed at 2 KHz with almost complete diffusion, while the diffusion is notably low at 100 Hz and 6350 Hz. Considering the simulation's sampling frequency of 32 KHz and the section on noise within the TLM, it becomes evident that results above 3200 Hz are highly affected by internal noise. To address this, a low-pass filter with a cut-off at $fs/10$ was applied. Despite this filtering, the results above 3200 Hz should be considered unreliable. Nonetheless, the diffusive properties exhibit high efficiency in the mid-range frequencies from 225-3150 Hz, indicating effective sound spreading by the diffusor across most of the frequency range. However, concerns arise for lower frequencies, particularly at 100 Hz, where the diffusion coefficient registers a value of 0.4. This discrepancy can be explained by considering the demands set forth by Equation (2.15) and Equation (2.13), where f_0 with the module's parameters is equal to 1003 Hz, resulting in f_{lower} being equal to 552 Hz. These findings substantiate the stability and efficiency of the simulated diffusion coefficient within a lower frequency range than theoretically calculated, with a consistent frequency range of 200-3150 Hz. Below this bound,

the diffusive properties exhibit significant variation and are not deemed stable, despite the exceptionally high values observed. A compelling diffusor should manifest a consistent diffusion coefficient within the given frequency range without huge fluctuations across the range.

4.4 Measurement

The measurements were carried out following the procedures outlined in Chapter 3. This section presents the results obtained from monitoring the environmental conditions in the anechoic and reverberation chambers. Additionally, it includes the post-processing of the measured data, resulting in the calculation of the directional diffusion coefficient and absorption coefficient for the module.

4.4.1 Environmental Conditions

Throughout the measurements conducted in both the reverberation chamber and the anechoic chamber, close attention was paid to environmental conditions, including temperature and humidity monitoring. In the anechoic chamber, the air conditioning was intentionally disabled to ensure a sound-free environment during measurements. However, some construction noise was detected during the time spent there. To minimize its impact, measurements were scheduled later in the day, after most construction activities were completed.

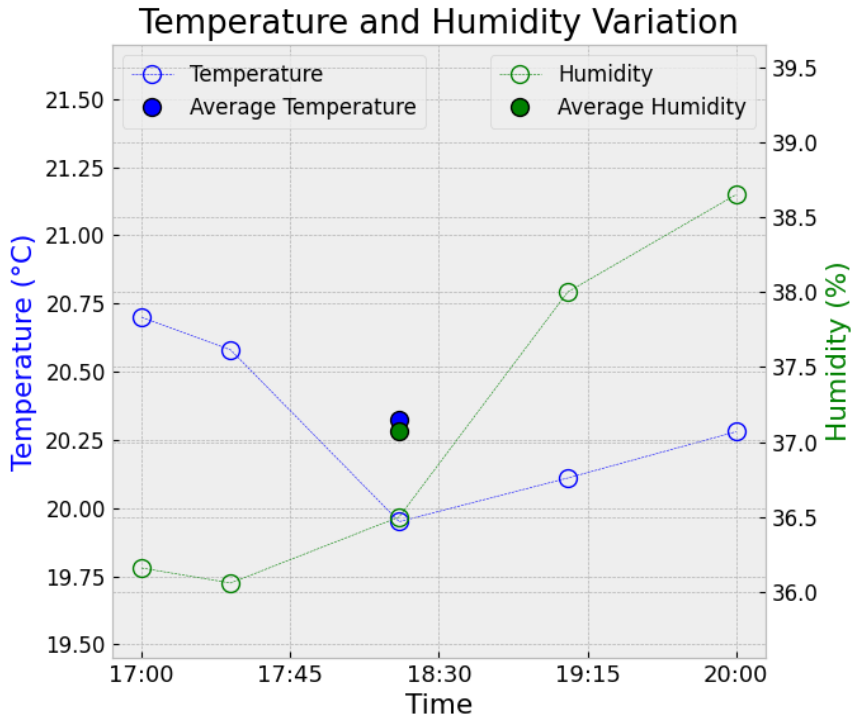

Figure 4.4.1: Temperature and humidity inside the anechoic chamber used for the directional diffusion coefficient measurements. Temperature is marked in blue and humidity in green. The axis on the left is related to temperature and the axis on the right to the humidity values.

In contrast, measurements inside the reverberation chamber presented a different challenge. Construction work was being carried out in the neighbouring room, and noise from this activity affected results if they where measuring at the same time as the noise was active, despite the presence of powerful speakers and significant sound pressure levels. Consequently, measurements were carefully conducted in-between the noisiest construction procedures. Each measurement was

therefore inspected for unwanted noise, and was repeated if the influence of noise was detected.

The recorded temperature and humidity values during the measurement series are depicted in Figure 4.4.1 for the anechoic chamber and Figure 4.4.2 for the reverberation chamber.

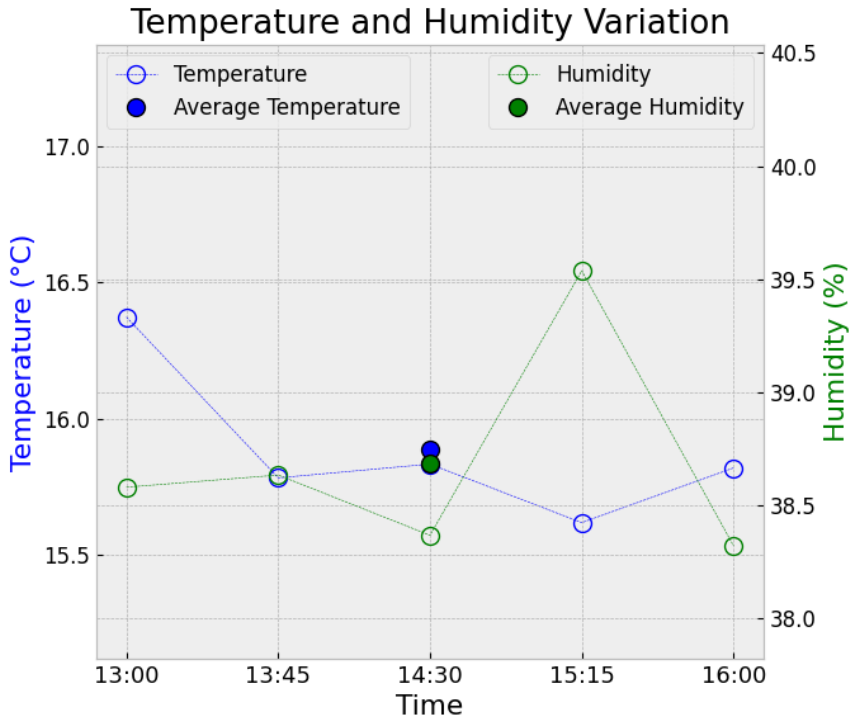

Figure 4.4.2: Temperature and humidity measurements inside the reverberation chamber during the absorption coefficient measurements. Temperature data is represented by the blue line, while humidity data is shown by the green line. The left axis is dedicated to temperature values, while the right axis corresponds to humidity values.

The temperature and humidity data exhibited relatively minor variances during the measurement series inside the anechoic chamber. The average temperature recorded was 20.32° with a variance of 0.079°, while the average humidity was 37.07% with a variance of 1.11%. External temperature fluctuations upon entering the room and the presence of an open window in the control room influenced the environmental conditions inside, but these changes did not significantly impact the measurements. Importantly, the observed temperature and humidity fluctuations remained well within the acceptable limits.

Within the reverberation room during measurements, a slight spike in humidity values occurred at 15:15, potentially due to increased human activity when moving the modules. However, this effect was minor in comparison to the overall variation, which could be attributed to the room's larger volume and the continuous operation of ventilation during measurements. Notably, the noise generated by the ventilation was considered part of the ambient background noise and did not influence the measurement results.

The average temperature recorded inside the reverberation room during mea-

surements was 15.89° with a variance of 0.06°, while the average humidity was 38.71% with a variance of 0.17%. These values align with the required temperature and humidity specifications outlined in the ISO 354:2004 standard, which require a temperature above 15° and a humidity between $30 - 90\%$, ensuring the reliability and accuracy of the experimental setup.

4.5 Directional Diffusion coefficient

Before processing the data obtained from measurements following ISO 17497-2:2012 guidelines, it was necessary to identify the time segment where the module's contribution was present. An example of the impulse response from the third measurement series is illustrated in Figure 4.5.1, where the time segment with the module's reflection is readily discerned, spanning from 18.8 ms to 21 ms. This distinction is apparent due to the clear separation between the red line, representing the impulse response with the module present, and the blue line, representing the reference impulse response without the module. The same process was repeated for each of the three individual measurement series to identify their respective time windows.

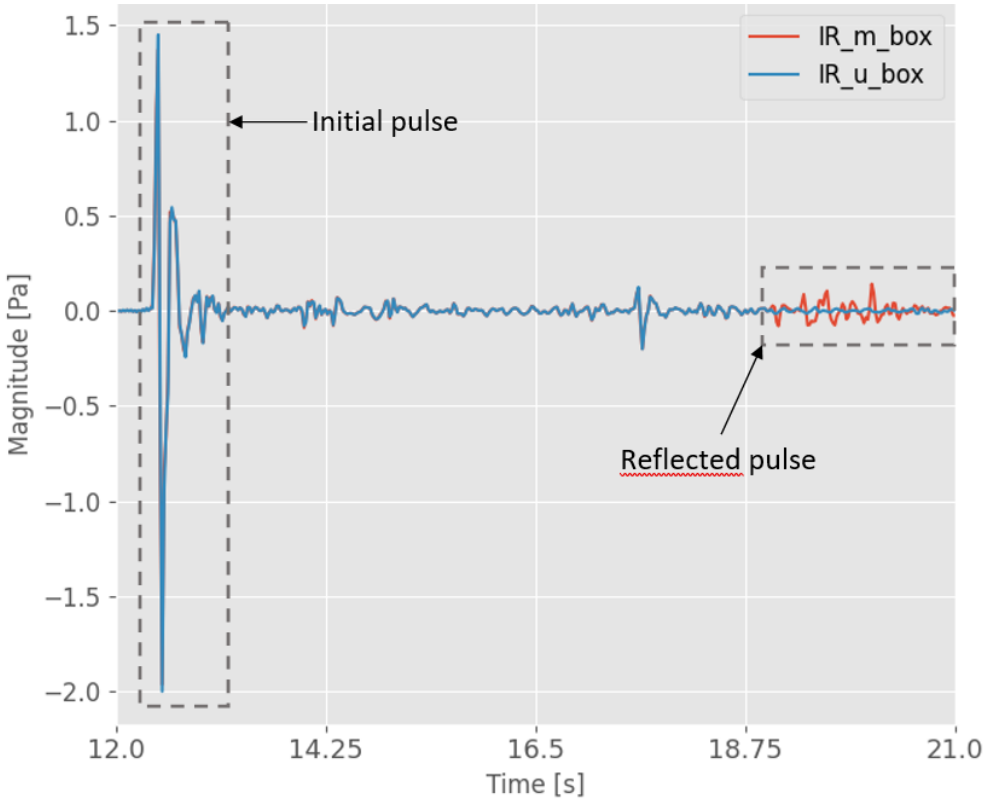

Figure 4.5.1: Impulse response for the third measurement series at -5°. The blue line is the impulse response without the module present, and the red line is with the module present.

Following the post-processing step, angular responses were generated for the three different measurement series. A total of 21 different one-third-octave bands were plotted, encompassing the frequency range from 100 Hz to 8 KHz, and can be found in Appendix B, C, and D for the three different measurement series.

The directive diffusion coefficient for the three measurement series is visualized in Figure 4.5.2, where (a) shows the raw, unfiltered diffusion coefficients, and (b) presents the polynomial fitted lines with an order of 10.

Upon inspecting the fitted lines in (b), it becomes evident that a common trend for all three curves is the high diffusion coefficient in the lower frequencies, followed by a decrease towards 1 KHz and then an increase towards 6.3 KHz. The most significant deviation is observed at 2 KHz, where the third measurement series, represented as the purple line, differs from the first- and second measurement series, marked respectively as the red and blue lines.

Further analysis of the real coefficient curves in (a) reveals a larger variation between the values. A shared feature among all curves is the high diffusive properties within the lower frequencies, followed by a decrease towards 1 KHz. Which was seen in (b). Both the red and purple lines show greater variations during the decrease towards 1 KHz, with the purple line exhibiting the largest fluctuations. In contrast, the blue line demonstrates a smoother decrease and a more consistent decreasing trend towards 1 KHz. However, after 2 KHz, the blue line also shows fluctuations similar to the ones displayed by the purple line at the lower frequencies.

The diffusion coefficient for the theoretical frequency range for the modules, calculated to be between 502-4513 Hz, is the highest for the blue and red lines, and lowest for the purple line. For the blue line, the coefficient values are above 0.59 for all frequencies within the theoretical range. For the red line, most of the values exceed 0.65, with the exception of 800 Hz, where it has a value of 0.52. In contrast, the purple line shows a larger deviation from the other two, with its lowest value at 0.46 within the theoretical frequency range.

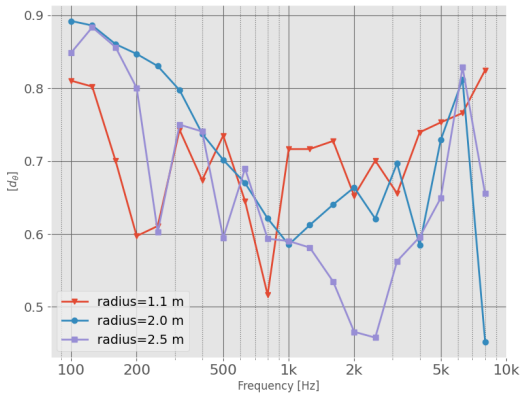

(a) Unfiltered.

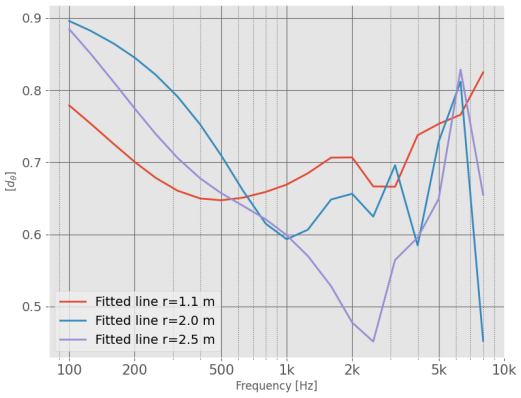

(b) Fitted lines with polynomial order of 10.

Figure 4.5.2: Calculated directional diffusion coefficient for the three different measurement series performed in the anechoic chamber. (a) show the unfiltered coefficient values and (b) display the polynomial fitted line related to the coefficient values.

In the analysis of Figure 4.5.3, showcasing the directivity for the three measurement series at 2 KHz, the frequency with the most significant deviation between the series, it becomes apparent that the third measurement series displays higher

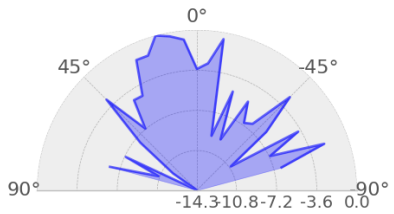

(a) First measurement series.

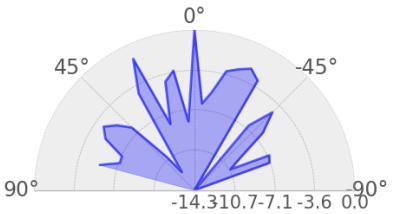

(b) Second measurement series.

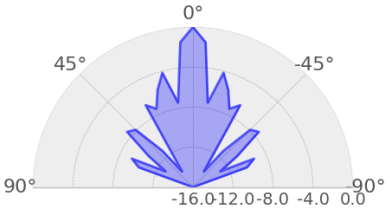

(c) Third measurement series.

Figure 4.5.3: Polar response of the module in the anechoic chamber at 2000 Hz for the three measurement series. (a) depicts the directivity at a radius of 1.1 m, (b) illustrates the same response at a radius of 2.0 m, and (c) displays the third measurement series at a radius of 2.5 m.

directivity, meaning less diffusion, compared to the first two measurement series. The directivity patterns for all three series show distinct sidelobes. For the third measurement series, the sidelobes are symmetrical around $\pm 65°$, $\pm 45°$, $\pm 30°$, and $\pm 15°$. In the second series, the sidelobes are slightly harder to separate due to larger variations, but they are still discernible at $-65°$, $-45°$, $\pm 25°$, $15°$, and $55°$. Some symmetry is evident, with the lobes slightly shifted from the mirrored $0°$.

In contrast, the first measurement series shows most of the values in the positive angular direction appearing merged. This pattern consistently persists throughout most of the polar plot results from this measurement series, raising the possibility of non-symmetrical attributes in the module or errors related to the measurement procedure. However, considering that this consistent error only occurs in the first measurement series, measurement errors are the most likely contributing factor. Nevertheless, upon inspecting the negative angular quadrant, distinct sidelobes can be located at $-70°$, $-45°$, $-20°$, and $-10°$. These findings demonstrate similarities with the sidelobes located in the other two measurement series, suggesting some consistency within the results, despite the presence of measurement errors.

4.6 Absorption coefficient

In the reverberation chamber, decay curves were measured to calculate both $T30$ and $T20$ values, despite the standard's specification to use $T20$. To obtain the absorption coefficient, the decay curves were averaged and Equation (3.1) was applied. Figure 4.6.1 displays the decay curves and corresponding absorption coefficient for the $T20$ results, while Figure 4.6.2 shows the values related to the $T30$ curves. Both measurement procedures are visualized in the graphs, with the case of treating the modules as a plane absorber marked as "plane absorber" and the set number of individual objects marked as "object." To better illustrate the trend of the absorption coefficients, two fitted lines of different orders were applied to find a smoothed average along the frequency spectrum.

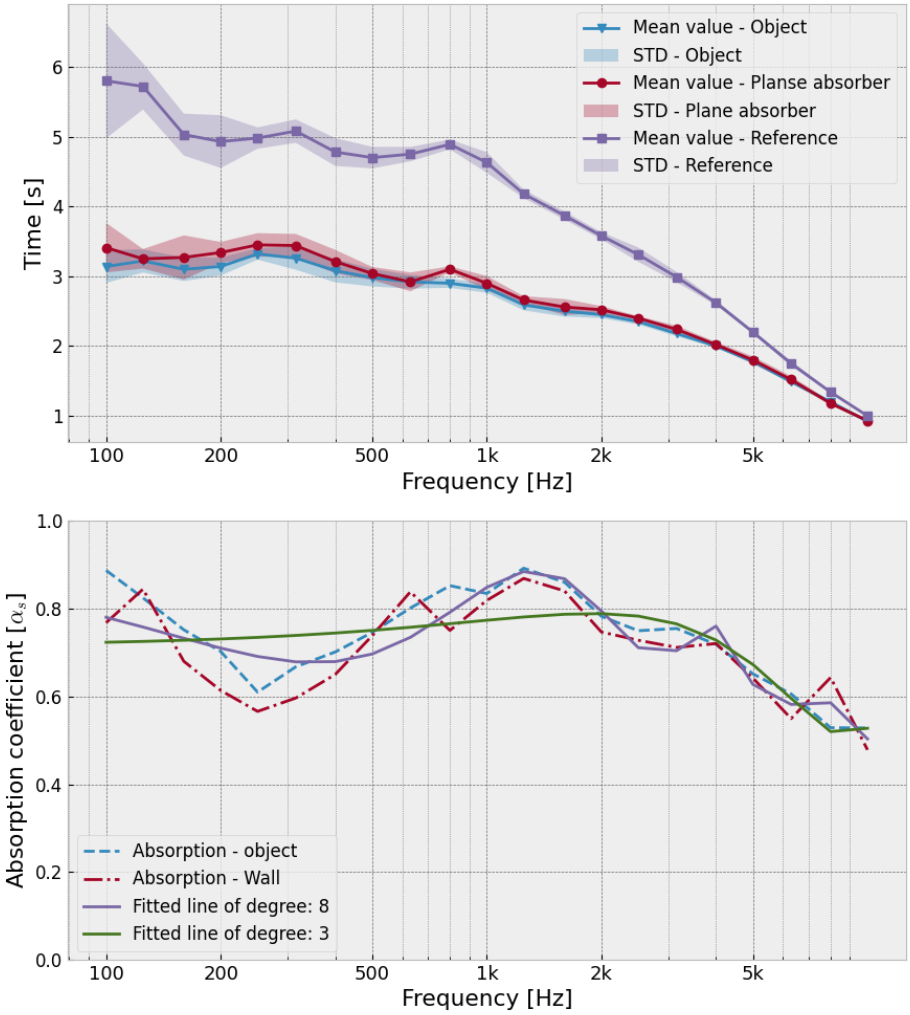

Figure 4.6.1: The top-most figure displays the average value of the $T20$ decay curves, with the standard deviation (STD) represented by the colored area. The bottom-most figure illustrates the absorption coefficient along with two fitted lines of different polynomial degrees (3 and 8).

Comparing the variances for the $T20$ and $T30$ values, it becomes evident that lower frequencies exhibit lower variance for $T20$, while higher frequencies show similar variances for both methods, with slightly less variance for $T30$. The two

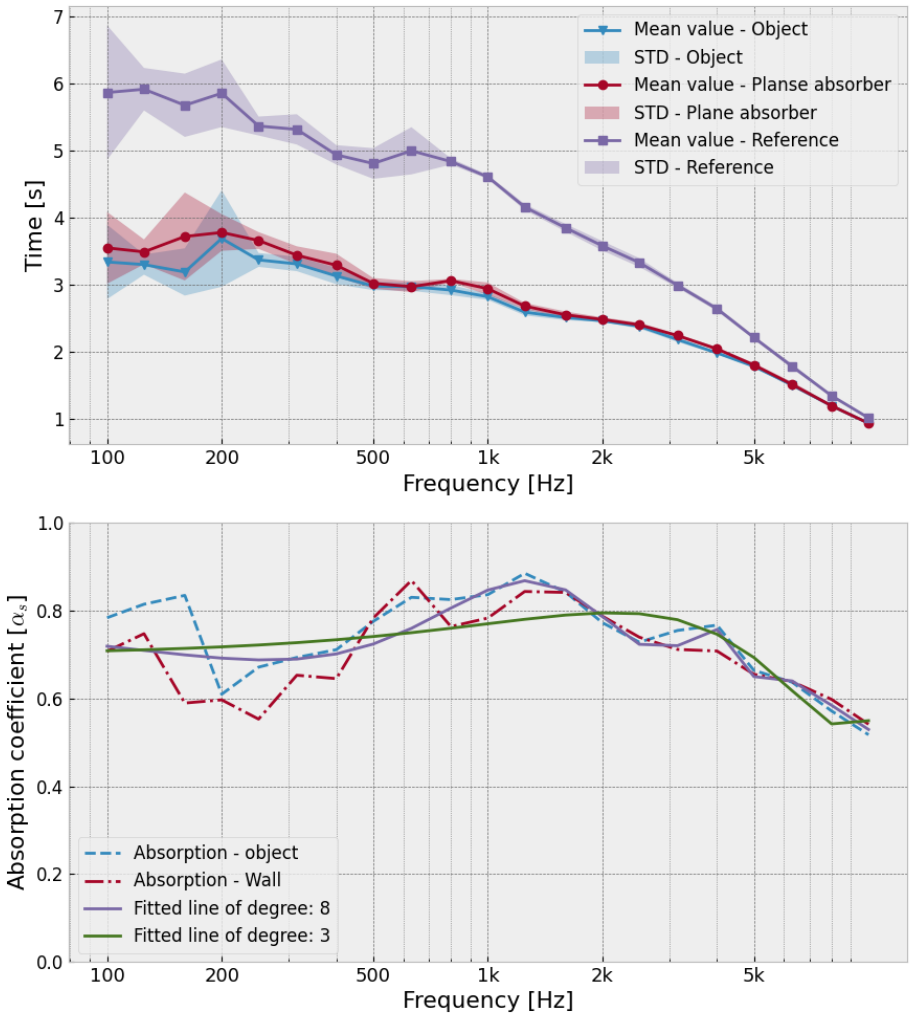

Figure 4.6.2: The top-most figure displays the average value of the $T30$ decay curves, with the standard deviation (STD) represented by the colored area. The bottom-most figure illustrates the absorption coefficient along with two fitted lines of different polynomial degrees (3 and 8).

reverberation time methods show relatively similar results, with the most significant difference observed at lower frequencies.

The room volume of the used reverberation chamber was 265.5 m^3, implying that the diffusive field within the room does not begin before 246 Hz, as stated by the Schroeder frequency[18]. This suggests the presence of stronger room modes for frequencies below the Schroeder frequency, which influence the reverberation time values in the lower frequency range of interest

Regarding the absorption coefficient for the modules, remarkable high values are observed for lower frequencies, averaging above 0.7 for most of the frequency range. Although these values are slightly reduced for higher frequencies, they still remain significant, gradually decreasing towards a value of 0.53.

The modules are designed with varying absorber thickness on different sides. The portion of the module with the QRD on top has an absorber thickness of 12 mm, while the larger box has an absorber thickness of 104 mm. The absorption characteristics differ across the frequency spectrum for these two thicknesses.

However, for the purpose of this thesis, the total absorption, combining both thicknesses, is more relevant since the modules operate as a cohesive unit rather than individually.

4.7 Measurements Compared to Simulated Results

4.7.1 Directional Diffusion Coefficient

The results from both the measurements and the simulation are display in Figure 4.7.1, showing (a) the raw data from the caclulations and (b) the fitted line to better identify trends when comparing the results. Comparing the results from the measured directional diffusion coefficient and the simulated directional diffusion coefficient, it is noticeable, if inspecting the results in (b) that the simulated results deviate significantly from the measured values. To some degree, it shows signs of being the inverse of the measured results. Between 100-315 Hz, the simulated results increase in value while the three measurement series decrease. At 2 KHz, the biggest deviation can be found, where the simulated results are above 0.94, differing from the third measurement series at 0.47. By then inspecting the values in (a), the similarities with the measured results are more significant. At 125 and 200 Hz, the simulated results deviate little from the measurement results, but at 100 and 150 Hz, the difference is vastly bigger. The variations in the simulated results at these lower frequencies variate from 0.4 to 0.83 between 100 and 125 Hz, before dropping down again at 150 Hz to 0.49. The huge fluctuation in values could be the result from strong interference but prove to make the simulated results less viable. Figure 4.7.1 show the averaged value for the measurement series with the standard deviation compared to the simulated values. Looking at the figure proves that little of the simulated results remain within the range of the measured results, proving the low accuracy of the simulated method compared to actual measurements. It validates the unreliability for the task of accurately describing the diffusive properties of the module using the TLM method constructed and should not be trusted as a viable simulation tool to test diffusive properties of different materials, sizes and QRD types for the modules before constructing them.

Figure 4.7.1 presents the results from both measurements and simulations, displaying (a) the raw data from the calculations and (b) the fitted line to better identify trends for comparison.

A notable observation when comparing the measured and simulated directional diffusion coefficients in (b) is that the simulated results significantly deviate from the measured values. In fact, the simulated results seem to exhibit an inverse trend compared to the measured results. Between 100-315 Hz, the simulated values increase while the three measurement series show a decreasing trend. At 2 KHz, the most significant deviation is observed, with the simulated results above 0.94, contrasting with the third measurement series at 0.47. Examining the values in (a) reveals some similarities with the measured results. At 125 and 200 Hz, the simulated values deviate only slightly from the measurement results, but at 100 and 150 Hz, the difference is notably larger. The simulated results at these lower frequencies fluctuate widely from 0.4 to 0.83 between 100 and 125 Hz, before dropping to 0.49 at 150 Hz. Such considerable fluctuations in values may indicate

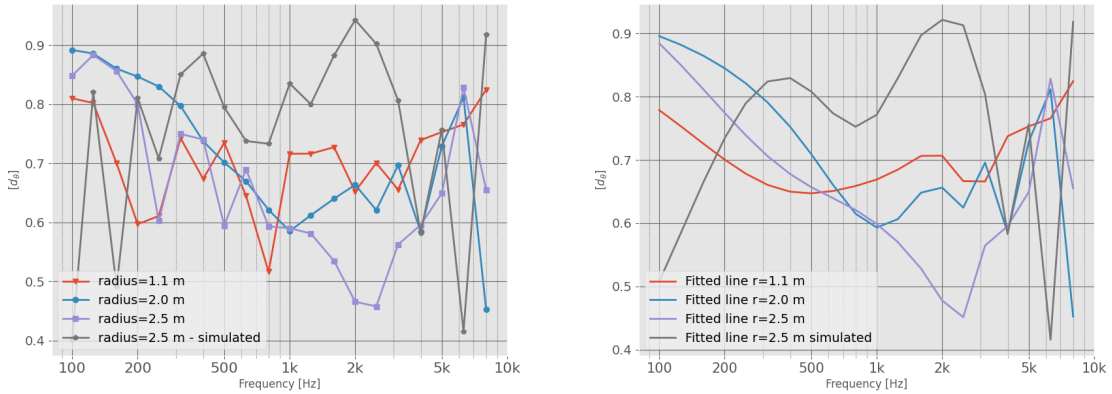

(a) Unfiltered. **(b)** Fitted lines with polynomial order of 10.

Figure 4.7.1: Calculated directional diffusion coefficient for the three different measurement series performed in the anechoic chamber, along with the simulated results. Figure (a) shows the unfiltered coefficient values, and Figure (b) displays the polynomial fitted line corresponding to the coefficient values.

strong interference but highlight the limited viability of the simulated results.

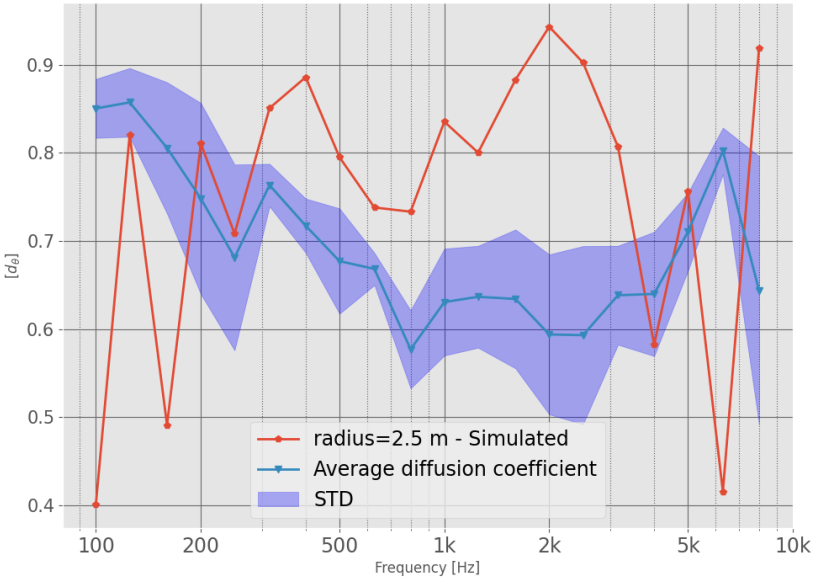

Figure 4.7.2: The averaged measured directional diffusion coefficients results with the standard deviation marked as the blue area, compared to the simulated results.

Figure 4.7.2 demonstrates the averaged value for the measurement series along with the standard deviation, compared to the simulated values. The figure clearly illustrates that the simulated results largely fall outside the range of the measured results, with only 5 out of 21 points within the blue area. This stark contrast

confirms the low accuracy of the simulated method compared to actual measurements.

These results validate the unreliability of the simulated method for accurately describing the diffusive properties of the module using the constructed TLM method. Therefore, it should not be relied upon as a viable simulation tool to assess the diffusive properties of different materials, sizes, and QRD types for the modules before construction.

If the simulation tools are to be used, a more comprehensive set of simulations, testing and comparisons of different modules must be conducted to better understand the errors and determine whether they are systematic or related to the simulation method applied.

4.8 Weaknesses related to TLM

The TLM technique offers distinct advantages over other simulation methods, particularly when dealing with parabolic equations. One key advantage is its unconditional stability, making it a useful tool in various operations.

However, the TLM technique is not without its challenges. Being a discrete technique, the wave emanating from a point source does not propagate uniformly. Additionally, the propagation speed in TLM is dependent on $1/\sqrt{2}$, which can have implications in specific applications. Understanding and addressing these limitations are crucial when choosing the appropriate method for modeling and simulating parabolic equation systems.

Upon processing the pressure data through a Fast Fourier Transform (FFT), the unevenness of frequencies within the grid becomes apparent, leading to the definition of a cut-off frequency critical for processing data from TLM simulations. The cut-off frequency, typically set at $fs/10$ or $fs/5.06$, limits the effective frequency range for the TLM model with an upper bound. This significantly impacts simulation speed, as the sampling frequency required for simulating the frequency of interest must be ten times larger than the upper frequency range of interest. While the high resolution yields detailed results, it also comes with increased simulation time. It should be noted that occasionally, stable outputs may be obtained even when exceeding the recommended limit, but this is mainly due to anti-aliasing effects and should never be considered a reliable solution.

CHAPTER

FIVE

CONCLUSIONS

5.1 Conclusion

This thesis embarked on evaluating Julia as a simulation tool for analyzing the acoustical properties of an innovative module constructed from recycled materials sourced from construction sites and buildings marked for demolition. The main objective involved developing a Transmission Line Matrix (TLM) model in Julia, capable of simulating the module's diffusive properties, while also performing empirical measurements on the physical modules.

The TLM model showcased its efficacy in accurately simulating certain room parameters, especially the reverberation time. However, when it came to representing the acoustical properties, particularly at specific frequencies, the model exhibited notable uncertainty. The root of this uncertainty can be attributed to simplifications made in the model's geometry, boundary conditions, grid resolution, and post-processing tools.

Comparing the measured results with the simulated outcomes explicitly highlighted that the applied TLM model is inadequate in representing the acoustical properties of the modules. Consequently, refinement and rework are imperative to enhance the model's accuracy and reliability in this specific context.

Notwithstanding the limitations of the simulation method, the measured absorption coefficient for the modules displayed promising outcomes. The average absorption coefficient consistently exceeded 0.7 for frequencies spanning from 100 Hz to 5000 Hz, indicating commendable sound absorption characteristics. Furthermore, the diffusion factor surpassed 0.6 within the relevant frequency range, signifying effective sound diffusion properties.

In conclusion, this thesis provided valuable insights into utilizing Julia as a simulation tool for assessing acoustical properties in modules constructed from recycled materials. While the TLM model demonstrated accuracy in certain room parameters, its shortcomings in accurately representing acoustical properties necessitate further refinements and improvements. The successful measurement of absorption coefficients and diffusion factors underscores the module's potential as an environmentally friendly and acoustically efficient interior solution. Future research should prioritize refining the simulation model to yield more precise results, thereby opening up opportunities for widespread application of these modules in various architectural and construction contexts.

5.2 Further Work

The results obtained from the absorption and diffusion tests conducted on the modules in this thesis demonstrate that the modules already function as reliable and effective interior components with desirable acoustical properties. However, significant improvements are needed in the simulation tools and methods applied to accurately simulate the measurement procedures.

To enhance the accuracy of the TLM method, better data processing methods and advanced rules should be implemented. This would result in more precise impulse responses and increased stability of the simulation results.

A potential improvement to the TLM simulation framework lies in integrating compatibility with CAD software or leveraging the Julia package GMSH. CAD software compatibility would streamline the process of defining the TLM grid by allowing direct import of complex geometries and structural models. Alternatively, leveraging GMSH capabilities within the TLM framework would enable more accurate simulations of intricate geometries and complex physical phenomena, expanding the tool's versatility for acoustic engineering applications.

Further improvements could be achieved by enhancing the treatment of absorption in the simulations, enabling simulation of the ISO 354:2003 standard and handling reflections and absorption for more complex structures with oblique incidents.

The current modules are constructed mainly from plywood and lumber, making them heavy and challenging to handle. Future work should focus on reducing the weight of the modules without compromising their acoustical performance and functionality.

To gather more comprehensive data on the acoustical properties of the modules, a more extensive test procedure should be implemented. This could involve using a larger anechoic chamber for the measurements related to ISO 17497-2:2012 to achieve optimal distance values.

Finally, conducting a test scenario where the modules are placed in music rehearsal rooms specifically designed for their purpose would provide valuable evidence of their impact on the acoustic environment. This would offer a more practical and tangible understanding of their effectiveness in real-world applications.

Overall, the future work should prioritize enhancing the simulation accuracy, optimizing the modules' weight and testing them in their intended settings to ensure they fulfill their acoustic objectives efficiently and reliably.

REFERENCES

[1] *ISO: 61672: Electroacoustics - Sound Level Meters - Part 1: Specifications*. 2003.

[2] *ISO 17497-2:2012, Sound Scattering Properties of Surfaces*. 2012.

[3] Kinsler Lawrence E. et al. *Fundamentals of Acoustics*. 4th. John Wiley & Sons, 2000. ISBN: 978-0-471-84789-2.

[4] Beranek Leo L. *Acoustics*. Acoustical Society of America, 2012.

[5] C. F Bohren and D. R Huffman. *Scattering fo Light by Small Particles*. Wiley-VCH. ISBN: 978-3527405035.

[6] Pierce Allan D. *Acoustics: An Introduction to its Physical Principles and Applications*. Acosutical Society of America, 1989.

[7] Kuttruff Heinrich. *Acoustics: An Introduction*. CRC Press, 2016.

[8] Morse Philip M. and Ingard K. Uno. *Theoretical Acoustics*. Princeton University Press, 1986.

[9] Rossing Thomas D. and Fletcher Neville H. *Principles of Vibration and Sound*. Springer Science & Business Media, 2013.

[10] Long Marshall. *Architectural acoustics*. 2nd. Elsevier Science & Technology, 2014. ISBN: 978-0-12-398258-2.

[11] Rossing Thomas D. *Springer Handbook of Acoustics*. 2nd. Springer-Verlag Berlin Heidelberg, 2014. ISBN: 978-1-4939-0754-0.

[12] Beranek Leo L. and Mellow Tim. *Acoustics: Sound Fields and Transducers*. Elsevier Science & Technology, 2012. ISBN: 978-0-12-391421-7.

[13] Miles Ronald N. *Physical Approach to Engineering Acoustics*. Springer, 2020. ISBN: 978-3-030-22675-6.

[14] And Leo L. *Concert Halls and Opera Houses: Music, Acoustics, and Architecture*. 2nd. Springer, 2004.

[15] Heinrich Kuttruff. *Room Acosutics*. 5th. Taylor & Francis, 2009.

[16] Wallace Clement Sabine. *Collected Papaers on Acoustics*. 2nd. Harvard University Press, 1922.

[17] *ISO 10534-2: Acoustics - Determination of Sound Absorption Coefficient and Impedance in Impedance Tubes: Transfer-Function Method*. 1998.

[18] F. Alton Everest and Ken C. Pohlmann. *Master Handbook of Acoustics*. 5th. McGraw-Hill, 2009. ISBN: 978-0-07-160332-4.

[19] *EASERA*. Berlin. URL: http://www.afmg.eu/en.

[20] Maryam Odabaee et al. "Modeling ultrasound propagation through material of increasing geometrical complexity". In: 90 (2018), pp. 52–62. URL: https://www.sciencedirect.com/science/article/%20pii/S0041624X17307850.

[21] Gerhard Müller and Michael Möser. *Handbook of Engineering Acoustics*. Springer-Verlag Berlin Heidelberg, 2013. ISBN: 978-3-540-24052-5.

[22] A. Bruce Carlson and Paul B. Crilly. *Communication Systems: An Introduction to Signals and Noise in Electrical Communication*. 5th. McGraw-Hill, 2010. ISBN: 978-0-07-338040-7.

[23] John G. Proakis and Dimitri G. Manolakis. *Digital Signal Processing: Principles, Algorithms, and Applications*. Pearson Education, 2006.

[24] Alan V. Oppenheim and Ronald W. Schafer. *Discrete-Time Signal Processing*. 3rd. Pearson Education, 2010.

[25] James W. Cooley and John W. Tukey. "An Algorithm for the Machine Calculation of Complex Fourier Series". In: *Mathematics of Computation* 19.90 (1965), pp. 297–301.

[26] Ronald N. Bracewell. *The Fourier Transform and it sApplications*. 3rd. McGraw-Hill, 2000.

[27] Finn Jacobsen and Peter Møller Juhl. *Fundamentals of General Linear Acoustics*. John Wiley & Sons, 2013. ISBN: 9781118636319.

[28] F. J. Harris. "On the use of windows for harmonic analysis with the discrete Fourier transform". In: *Proceedings of the IEEE* 66.1 (1978), pp. 51–83.

[29] J. W. Tukey. "The Practical Relationship between Spectrum Analysis and Spectral Analysis." In: *Proceedings of the IEEE* 70.11 (1982), pp. 1055–1056.

[30] Julius O. Smith. "Introduction to Digital Filters with Audio Applications". In: (). URL: https://ccrma.stanford.edu/~jos/filters/.

[31] Cox Trevor J and D'Antonio Peter. *Acoustic absorbers and diffusers: Theory, design and application*. CRC Press, 2016.

[32] Peter P. Mondrian and Russel J. Mason. "Diffuse Sound Reflection by Maximum-Length Sequences and Quadratic Residues". In: *The Journal of the Acoustical Society of America* 78.1 (1985), pp. 243–247. DOI: 10.1121/1.392800.

[33] *Lydspredende flater (diffusorer)*. Norsk. 1999.

[34] Y. Kagawa et al. "Discrete Huygens´ Model Approach to Sound Wave Propagation". In: *Journal of Sound and Vibration* 218(3).sv981861 (June 1998), pp. 419–444.

[35] Peter B. Johns. "Numerical Electromagnetism: The Transmission Line Matrix Method". In: *Wiley-IEEE Press* (1991).

[36] Cheng An-Ming. *Field and Wave Electromagnetics*. 2nd. Pearson Education, 2005.

[37] C. A. Brebbia. *Boundary Elements: An Introductory Course*. 2nd. WIT Press, 2012.

[38] Hughes Thomas J. R. *The Finite Element Method: Linear Static and Dynamic Finite Element Analysis*. Doved Ed. Dover Publications, 2012.

[39] Guillaume Dutilleux and J Waechter. "The TLM method for acoustics: local and distributed implementations in Scilab". In: (July 2023).

[40] Juan Morente, Jorge Portí, and Mohsine Khalladi. "Absorbing Boundary Conditions for the TLM Method". In: *Microwave Theory and Techniques, IEEE Transactions on* 40 (Dec. 1992), pp. 2095–2099. DOI: 10.1109/22.168768.

[41] Jeff Bezanson et al. "Julia: A Fresh Approach to Numerical Computing". In: *SIAM Review* 59.1 (2017), pp. 65–98. DOI: 10.1137/141000671.

[42] *Python*. URL: https://docs.python.org/.

[43] Siu Kwan Lam, Avik Sengupta, and Lorena A. Barba. "Numba: A LLVM-Baset Python JIT Compiler". In: *Proceedings of the Second Workshop on the LLVM Compiler Infrastructure in HPC (LLVM-HPC)* (2015), pp. 7–16. URL: https://dl.acm.org/doi/10.1145/2833157.2833162.

[44] John P. Bentley. *Principles of Measurement Systems*. 4th. Pearson Education, 2005. ISBN: 978-0-13-043028-1.

[45] *Guide 98-3 Uncertainty of Measurements*. 2008.

[46] R. V. Hogg, J. McKean, and A. T. Craig. *Introduction to Mathematical Statistics*. 8th. Pearson Education, 2018.

[47] D. C Montgomery, G. C. Runger, and N. F Hubele. *Engineering Statistics*. 5th. John Wiley & Sons, 2012.

[48] *Measurement of sound absorption properties of road surfaces in situ - Part 1: Roadside Method*. 2010.

[49] Xiang Duanqi, Wang Zheng, and Chen Jinjing. "Acoustic Design of an Anechoic Chamber". In: *Applied Acoustics* 29.2 (1990), pp. 129–149. URL: https://www.sciencedirect.com/science/article/abs/pii/0003682X9090027R.

[50] Singh K. Sushil, Mohit Garg, and S. Narayanan. "Estimation of the Lower cut-off Frequency of an Anechoic Chamber: An Empirical Approach". In: *International Journal of Acoustics* 19 (2020), pp. 57–72. URL: https://journals.sagepub.com/doi/10.1177/1475472X20905070.

[51] Isabel Expósito, Manual García Sánches, and Iñigo Cuiñas. "Uncertainty Assessment of a Small Rectangular Anechoic Chamber: From Design to Operation." In: *IEEE* 68.6 (2020), pp. 4871–4880. URL: https://ieeexplore.ieee.org/document/8979259.

[52] Kuttruff Heinrich. *Room acoustics*. 6th ed. CRC Press, 2016.

[53] Duttileux Guilaume and Wachter J. "The TLM Method for Acoustics: Local and Distributed Implementations in Scilab". In: ().

APPENDICES

APPENDIX

A

GITHUB REPOSITORY

All code and figures used in this document are included in the Github repository linked below as well as additional material. Further explanations are given in the readme-file.

Github repository link

- `https://github.com/erlenkb/TFE4940_Master_Thesis`

APPENDIX

B

DIRECTIVITY PLOTS FROM THE FIRST MEASUREMENT SERIES FOLLOWING ISO 17497-2:2012

B1 - Angular Directivity Plot for the First Measurement Series (100-200 Hz)

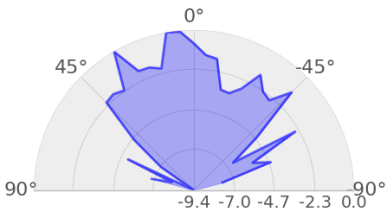

(a) Frequency = 100 Hz.

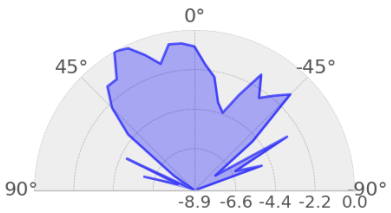

(b) Frequency = 125 Hz.

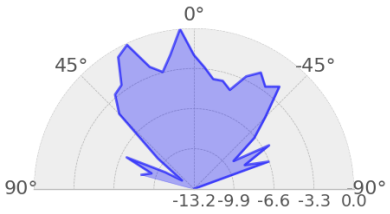

(c) Frequency = 150 Hz.

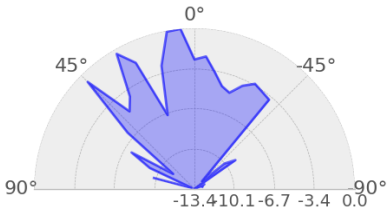

(d) Frequency = 200 Hz.

Figure B.1: The images display the angular directivity of the modules, measured at a distance of 1.1 meters, within the third-octave bands ranging from 100 Hz to 250 Hz.

B2 - Angular Directivity Plot for the First Measurement Series (250-500Hz)

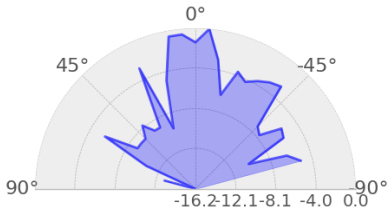

(a) Frequency = 250 Hz.

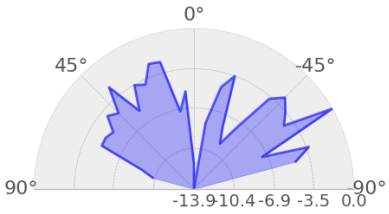

(b) Frequency = 315 Hz.

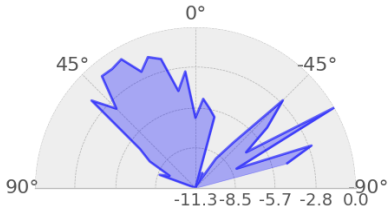

(c) Frequency = 400 Hz.

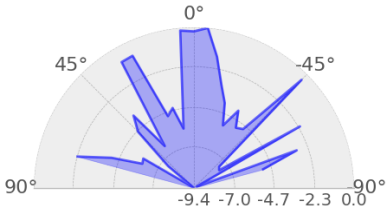

(d) Frequency = 500 Hz.

Figure B.2: The images display the angular directivity of the modules, measured at a radius of 1.1 meters, within the third-octave bands ranging from 250 Hz to 5000 Hz.

B3 - Angular Directivity Plot for the First Measurement Series (630-1250 Hz)

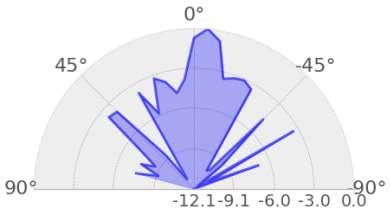

(a) Frequency = 630 Hz.

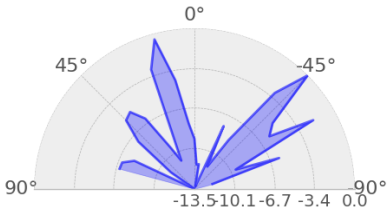

(b) Frequency = 800 Hz.

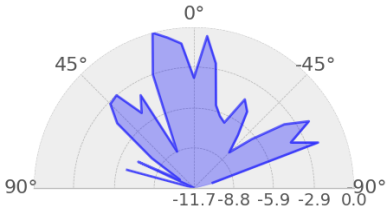

(c) Frequency = 1000 Hz.

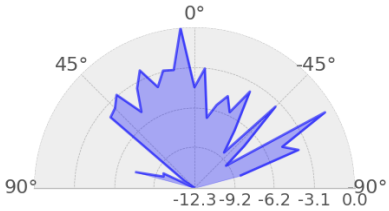

(d) Frequency = 1250 Hz.

Figure B.3: The images display the angular directivity of the modules, measured at a distance of 1.1 meters, within the third-octave bands ranging from 630 Hz to 1250 Hz.

B4 - Angular Directivity Plot for the First Measurement Series (1600-3150 Hz)

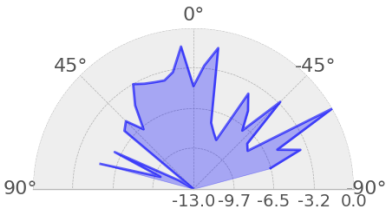

(a) Frequency = 1600 Hz.

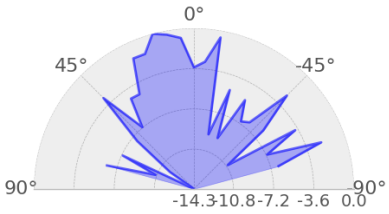

(b) Frequency = 2000 Hz.

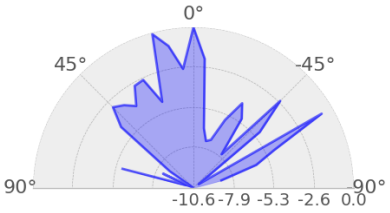

(c) Frequency = 2500 Hz.

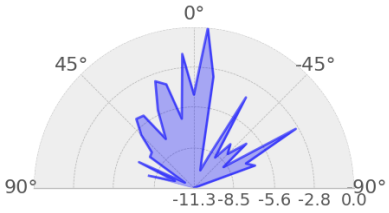

(d) Frequency = 3150 Hz.

Figure B.4: The images display the angular directivity of the modules, measured at a distance of 1.1 meters, within the third-octave bands ranging from 1600 Hz to 3150 Hz.

B5 - Angular Directivity Plot for the First Measurement Series (4000-8000 Hz)

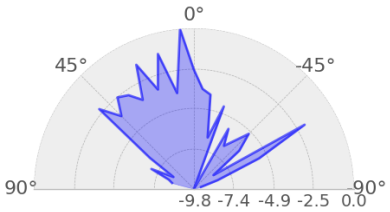

(a) Frequency = 4000 Hz.

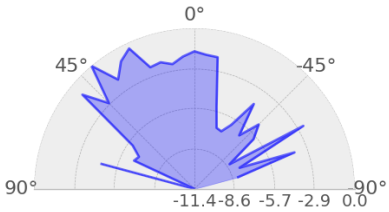

(b) Frequency = 5000 Hz.

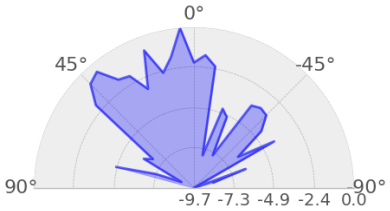

(c) Frequency = 6300 Hz.

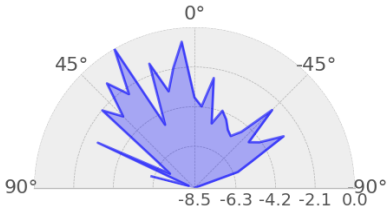

(d) Frequency = 8000 Hz.

Figure B.5: The images display the angular directivity of the modules, measured at a distance of 1.1 meters, within the third-octave bands ranging from 4000 Hz to 8000 Hz.

APPENDIX

C

DIRECTIVITY PLOTS FROM THE SECOND MEASUREMENT SERIES FOLLOWING ISO 17497-2:2012

C1 - Angular Directivity Plot for the Second Measurement Series (100-200 Hz)

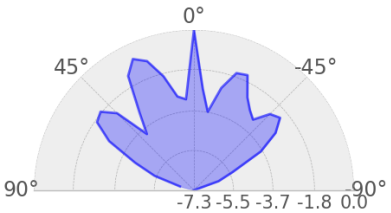

(a) Frequency = 100 Hz.

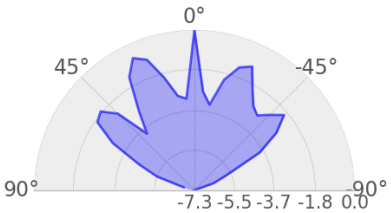

(b) Frequency = 125 Hz.

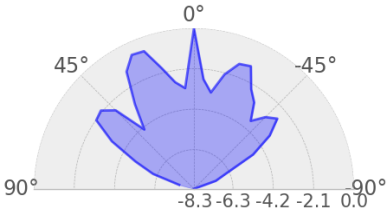

(c) Frequency = 150 Hz.

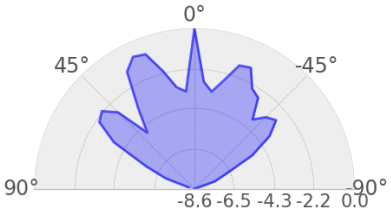

(d) Frequency = 200 Hz.

Figure C.1: The images display the angular directivity of the modules, measured at a distance of 1.1 meters, within the third-octave bands ranging from 100 Hz to 259 Hz.

C2 - Angular Directivity Plot for the Second Measurement Series (250-500Hz)

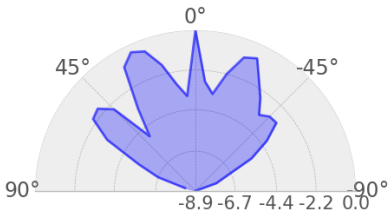

(a) Frequency = 250 Hz.

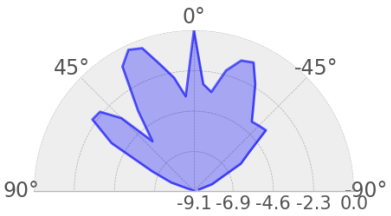

(b) Frequency = 315 Hz.

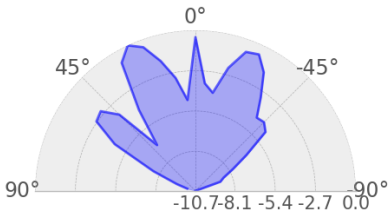

(c) Frequency = 400 Hz.

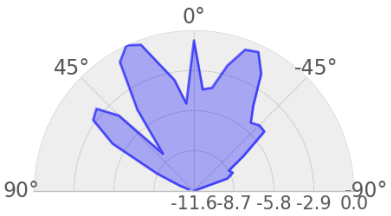

(d) Frequency = 500 Hz.

Figure C.2: The images display the angular directivity of the modules, measured at a distance of 1.1 meters, within the third-octave bands ranging from 250 Hz to 500 Hz.

C3 - Angular Directivity Plot for the Second Measurement Series (630-1250 Hz)

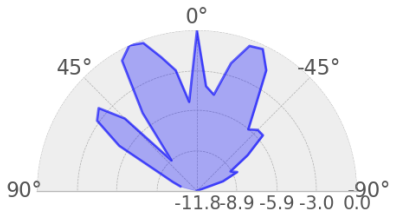

(a) Frequency = 630 Hz.

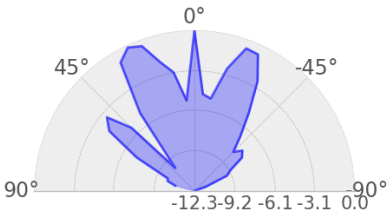

(b) Frequency = 800 Hz.

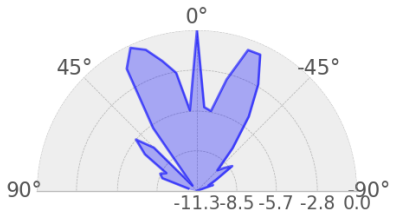

(c) Frequency = 1000 Hz.

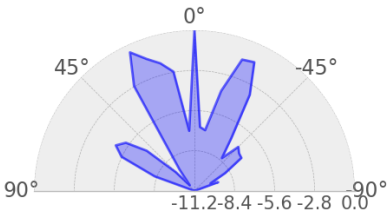

(d) Frequency = 1250 Hz.

Figure C.3: The images display the angular directivity of the modules, measured at a distance of 1.1 meters, within the third-octave bands ranging from 630 Hz to 1250 Hz.

C4 - Angular Directivity Plot for the Second Measurement Series (1600-3150 Hz)

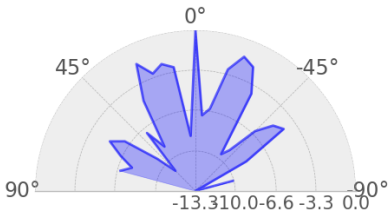

(a) Frequency = 1600 Hz.

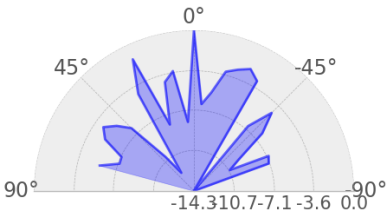

(b) Frequency = 2000 Hz.

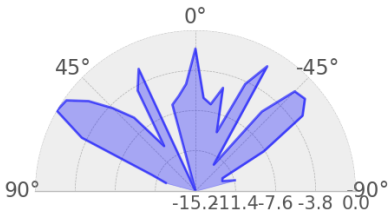

(c) Frequency = 2500 Hz.

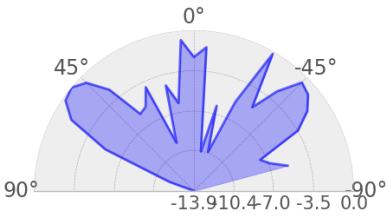

(d) Frequency = 3150 Hz.

Figure C.4: The images display the angular directivity of the modules, measured at a distance of 1.1 meters, within the third-octave bands ranging from 1600 Hz to 3150 Hz.

C5 - Angular Directivity Plot for the Second Measurement Series (4000-8000 Hz)

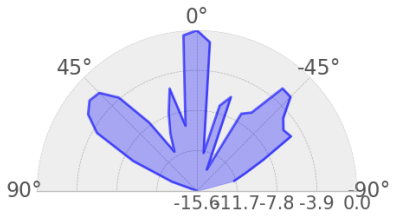

(a) Frequency = 4000 Hz.

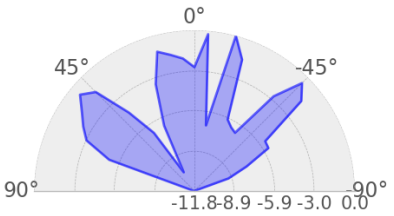

(b) Frequency = 5000 Hz.

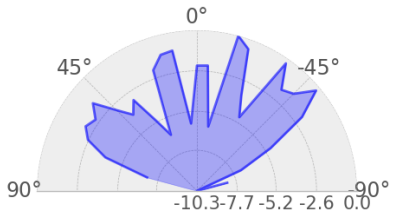

(c) Frequency = 6300 Hz.

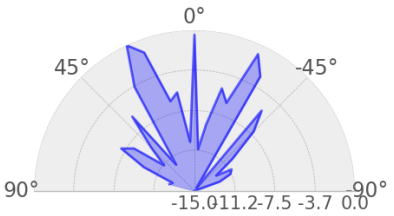

(d) Frequency = 8000 Hz.

Figure C.5: The images display the angular directivity of the modules, measured at a distance of 1.1 meters, within the third-octave bands ranging from 4000 Hz to 8000 Hz.

APPENDIX

D

DIRECTIVITY PLOTS FROM THE THIRD MEASUREMENT SERIES FOLLOWING ISO 17497-2:2012

D1 - Angular Directivity Plot for the Third Measurement Series (100-200 Hz)

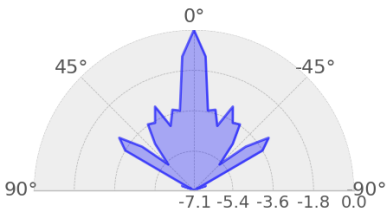

(a) Frequency = 100 Hz.

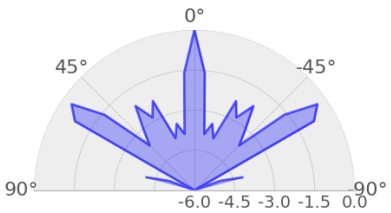

(b) Frequency = 125 Hz.

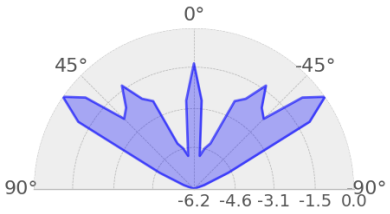

(c) Frequency = 150 Hz.

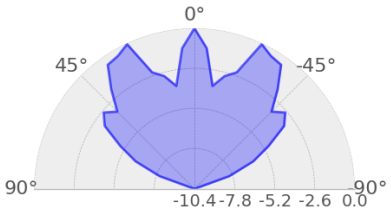

(d) Frequency = 200 Hz.

Figure D.1: The images display the angular directivity of the modules, measured at a distance of 1.1 meters, within the third-octave bands ranging from 250 Hz to 500 Hz.

D2 - Angular Directivity Plot for the Third Measurement Series (250-500Hz)

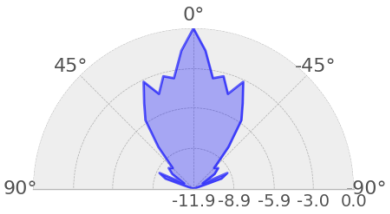

(a) Frequency = 250 Hz.

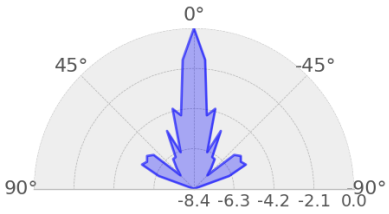

(b) Frequency = 315 Hz.

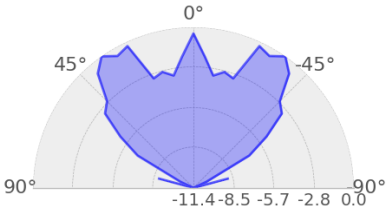

(c) Frequency = 400 Hz.

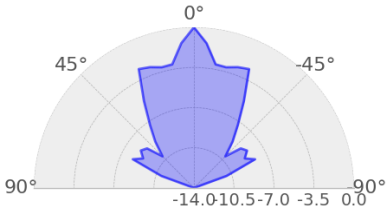

(d) Frequency = 500 Hz.

Figure D.2: The images display the angular directivity of the modules, measured at a distance of 1.1 meters, within the third-octave bands ranging from 100 Hz to 200 Hz.

D3 - Angular Directivity Plot for the Third Measurement Series (630-1250 Hz)

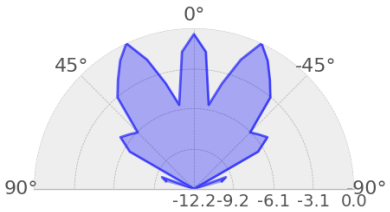

(a) Frequency = 630 Hz.

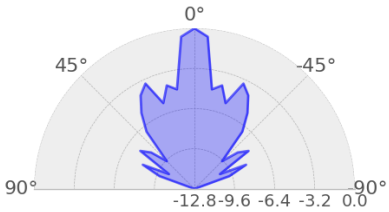

(b) Frequency = 800 Hz.

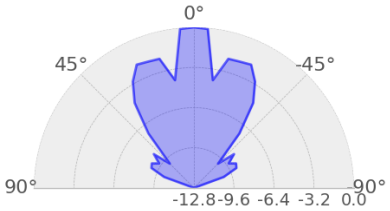

(c) Frequency = 1000 Hz.

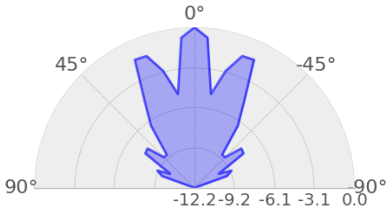

(d) Frequency = 1250 Hz.

Figure D.3: The images display the angular directivity of the modules, measured at a distance of 1.1 meters, within the third-octave bands ranging from 630 Hz to 1250 Hz.

D4 - Angular Directivity Plot for the Third Measurement Series (1600-3150 Hz)

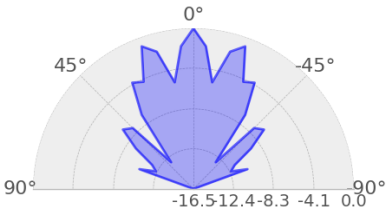

(a) Frequency = 1600 Hz.

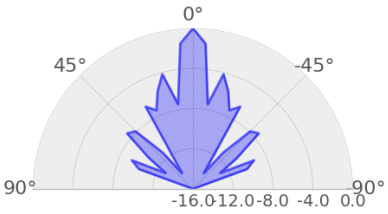

(b) Frequency = 2000 Hz.

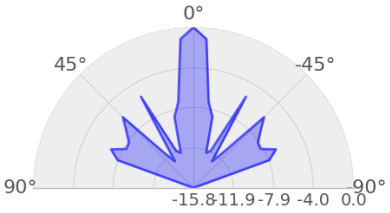

(c) Frequency = 2500 Hz.

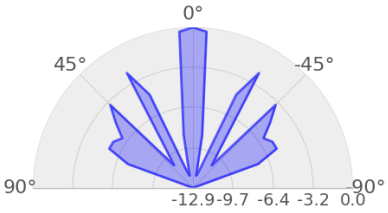

(d) Frequency = 3150 Hz.

Figure D.4: The images display the angular directivity of the modules, measured at a distance of 1.1 meters, within the third-octave bands ranging from 1600 Hz to 3150 Hz.

D5 - Angular Directivity Plot for the Third Measurement Series (4000-8000 Hz)

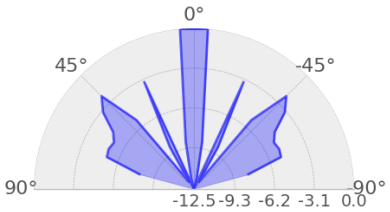

(a) Frequency = 4000 Hz.

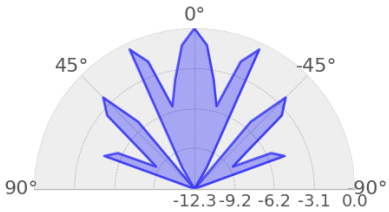

(b) Frequency = 5000 Hz.

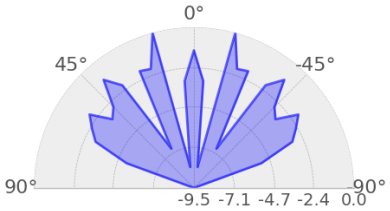

(c) Frequency = 6300 Hz.

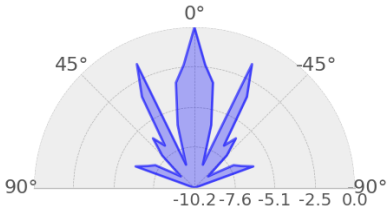

(d) Frequency = 8000 Hz.

Figure D.5: The images display the angular directivity of the modules, measured at a distance of 1.1 meters, within the third-octave bands ranging from 4000 Hz to 8000 Hz.

APPENDIX

E

DIRECTIVITY PLOTS FROM THE SIMULATED MEASUREMENT SERIES FOLLOWING ISO 17497-2:2012

E1 - Angular Directivity Plot for the Simulated Series (100-200 Hz)

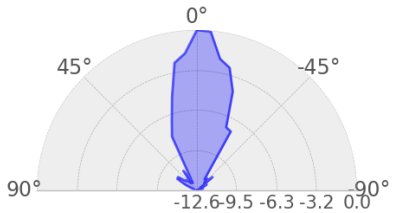

(a) Frequency = 100 Hz.

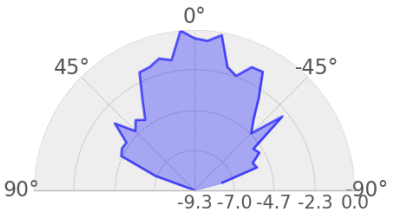

(b) Frequency = 125 Hz.

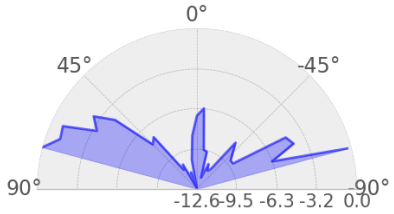

(c) Frequency = 150 Hz.

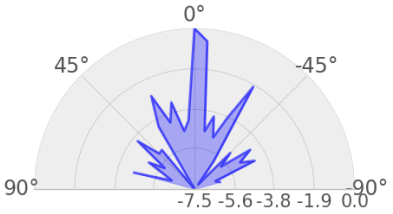

(d) Frequency = 200 Hz.

Figure E.1: The images display the angular directivity of the modules, simulated with a measuring distance from the module of 2.5 meters, within the third-octave bands ranging from 100 Hz to 200 Hz.

E2 - Angular Directivity Plot for the Simulated Series (250-500Hz)

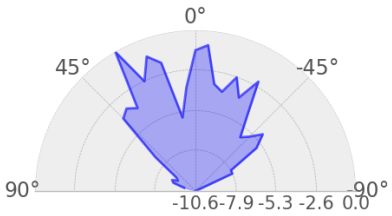

(a) Frequency = 250 Hz.

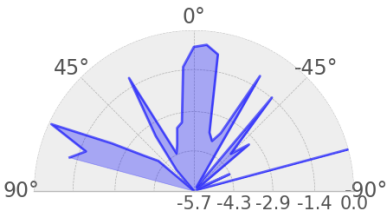

(b) Frequency = 315 Hz.

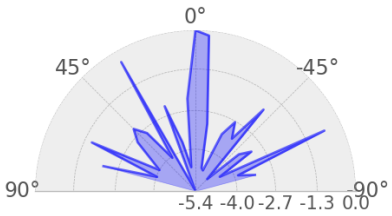

(c) Frequency = 400 Hz.

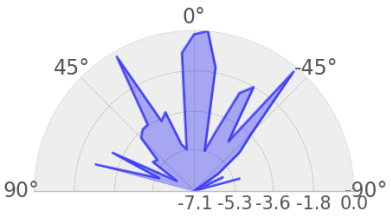

(d) Frequency = 500 Hz.

Figure E.2: The images display the angular directivity of the modules, simulated with a measuring distance from the module of 2.5 meters, within the third-octave bands ranging from 250 Hz to 500 Hz.

E3 - Angular Directivity Plot for the Simulated Series (630-1250 Hz)

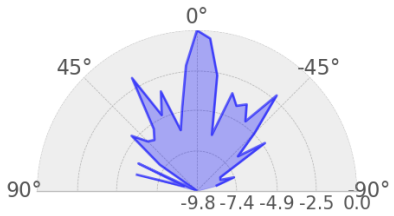

(a) Frequency = 630 Hz.

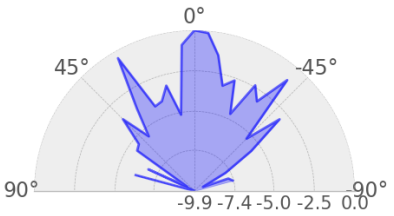

(b) Frequency = 800 Hz.

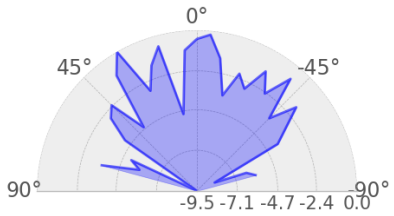

(c) Frequency = 1000 Hz.

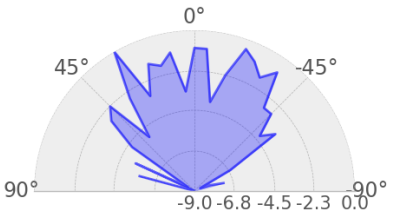

(d) Frequency = 1250 Hz.

Figure E.3: The images display the angular directivity of the modules, simulated with a measuring distance from the module of 2.5 meters, within the third-octave bands ranging from 630 Hz to 1250 Hz.

E4 - Angular Directivity Plot for the Simulated Series (1600-3150 Hz)

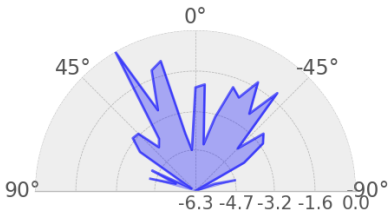

(a) Frequency = 1600 Hz.

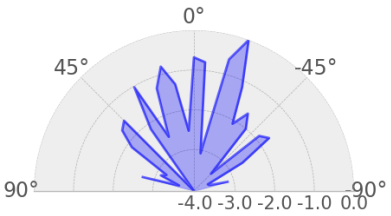

(b) Frequency = 2000 Hz.

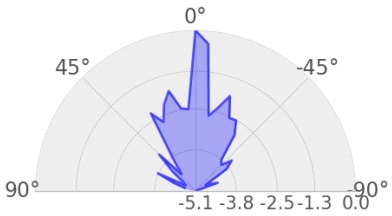

(c) Frequency = 2500 Hz.

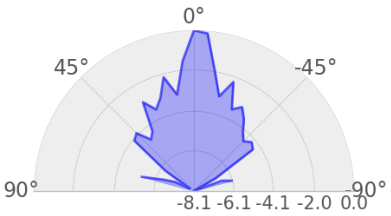

(d) Frequency = 3150 Hz.

Figure E.4: The images display the angular directivity of the modules, simulated with a measuring distance from the module of 2.5 meters, within the third-octave bands ranging from 1600 Hz to 3150 Hz.

E5 - Angular Directivity Plot for the Simulated Series (4000-8000 Hz)

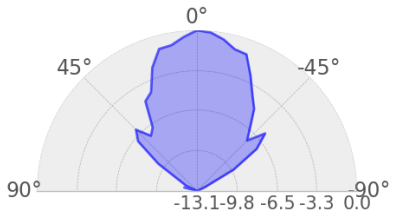

(a) Frequency = 4000 Hz.

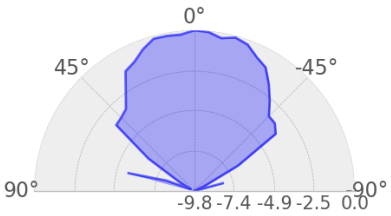

(b) Frequency = 5000 Hz.

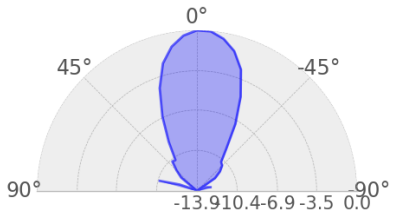

(c) Frequency = 6300 Hz.

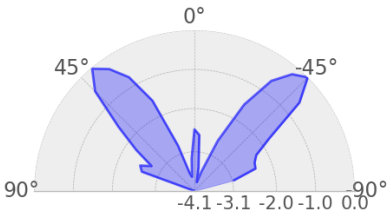

(d) Frequency = 8000 Hz.

Figure E.5: The images display the angular directivity of the modules, simulated with a measuring distance from the module of 2.5 meters, within the third-octave bands ranging from 4000 Hz to 8000 Hz.

NTNU
Norwegian University of
Science and Technology

RAMBØLL